The International Journal of Advanced Manufacturing Technology
https://doi.org/10.1007/s00170-025-16921-w

ORIGINAL ARTICLE

Influence of tube arrangement and core types on the crushing performance of core-filled nested and adjoined structures

ThanhSon Doan[1] · Arun Arjunan[2] · TrongNhan Tran[3] · Quirino Estrada[4] · Ameen Topa[5] · PhucThien Nguyen[6]

Received: 1 May 2025 / Accepted: 30 October 2025

Abstract
This study investigates the influence of tube arrangement and core filling on the crashworthiness performance of three tube architectures namely nested (NRT and NST), single (SingleT) and adjoined (ART). Experimental and numerical analyses, along with a Random Forest machine learning model, were employed to investigate their response under crushing conditions. Unfilled NRT and NST tubes demonstrated notably higher mean crushing load (MCL) and crushing load ratio (CLR) compared to SingleT and ART, with increases of 69.8% and 17.14% for MCL and 85.55% and 60.77% for CLR, respectively. The Entropy-EDAS method highlighted NST1 as the most effective unfilled design. For core-filled tubes, the crashworthiness was governed by a combination of tube arrangement, cross-sectional geometry and core filling. However, in unfilled samples, only the tube arrangement and cross-section played a significant role in the crash behavior. Among the core-filled samples, ART structures exhibited superior improvements in CLR and crushing behavior compared to their unfilled counterparts, with perpendicular arrangements showing the most significant enhancement. The specific energy absorption (SEA) of ART1(FEA) and ART2(FEA) core-filled tubes surpassed their unfilled counterparts by approximately 26.84% and 40.36%, respectively. Furthermore, core type 2 (C2) consistently outperformed core type 1 (C1), with ART2(FEA)_C2 showing a 12–14% improvement in crashworthiness metrics. The integration of materials with varying Young's moduli, such as combining ART tubes with ABS cores, was found to significantly enhance crashworthiness, particularly when the tubes were arranged perpendicularly.

Keywords Crashworthiness · Machine learning · Additive manufacturing · Multi-objective decision making · Thin-walled tube

1 Introduction

Thin-walled structures have emerged as preeminent solutions for energy absorption applications across various transportation sectors, including railway systems, aerospace engineering and electric vehicle manufacturing, primarily due to their exceptional energy absorption characteristics. Recent investigations have explored a diverse array of thin-walled structural configurations, encompassing various cross-sectional geometries: triangular Sect [1]., square Sect [2]., elliptical profile [3], circular configuration [4], hexagonal Sect [5]. and star-shaped tube [6]. The other studies

✉ TrongNhan Tran
trantrongnhan@iuh.edu.vn

ThanhSon Doan
son.dt@vlu.edu.vn

[1] Faculty of Automotive Engineering, Van Lang School of Technology, Van Lang University, Ho Chi Minh City, Vietnam

[2] Centre for Engineering Innovation and Research (CEIR), School of Engineering, University of Wolverhampton, Telford Innovation Campus, Telford TF29NT, UK

[3] Faculty of Mechanical Engineering, Industrial University of Ho Chi Minh City, Ho Chi Minh City, Vietnam

[4] Instituto de Ingeniería y Tecnología, Universidad Autónoma de Ciudad Juárez (UACJ), Ciudad Juárez, Chihuahua, México

[5] Department of Maritime Technology, Faculty of Ocean Engineering Technology, Universiti Malaysia Terengganu, Kuala Terengganu, Malaysia

[6] Faculty of Engineering and Technology, Van Hien University, Ho Chi Minh City, Vietnam

Published online: 19 November 2025

have been further expanded to examine multiple material compositions, including composites [7], steel [8], magnesium alloy [9] or aluminum alloy [10], each offering distinct advantages for specific applications. The behavioral characteristics of these structures have been extensively analyzed under numerous loading conditions, including axial load [11, 12], oblique load [13], or lateral load [14, 15]. Additionally, significant research efforts have been directed toward understanding their responses under dynamic conditions, particularly focusing on impact and impulsive loading phenomena [16–18]. The diverse range of performances exhibited by these various configurations, while offering extensive design possibilities, presents a considerable challenge for designers attempting to identify optimal solutions for specific crashworthiness applications.

Within the realm of thin-walled structure research, investigations centered on axial loading conditions have garnered significant attention, primarily attributed to its demonstrated superior energy absorption characteristic in comparison to lateral or oblique loading conditions. This research emphasis has generated a comprehensive array of studies examining the crashworthiness behavior of axially compressed structures, encompassing numerical [19] and theoretical [20] approaches.

In the pursuit of enhanced energy absorption under axial loading conditions, researchers have explored a diverse array of innovative design strategies, encompassing nested structures [21], multi-cell [22], or foam-filled [23] approaches, each offering unique advantages in crashworthiness. Nia and Chahardoli [24] undertook a comprehensive evaluation of nested tube assemblies with varying numbers of components, establishing a direct correlation between the quantity of constituent tubes and enhanced energy absorption capabilities. Complementing this line of research, Acar et al. [25] undertook an evaluation of multi-cell tube crashworthiness, employing two pivotal performance metrics—crush force efficiency and specific energy absorption—to formulate design recommendations that advocate for the strategic reduction of wall thickness and augmentation of diameter to optimize crashworthy performance.

Reddy and Wall's [26] exploration of foam-filled circular tubes under axial loading highlighted the critical role of foam density in modulating both energy absorption capacity and the fundamental mode of collapse, underscoring the intricate interplay between material properties and mechanical behavior in composite tubular structures. Expanding on these studies, Wang et al. [27] investigated the performance modifications achieved through the integration of aluminum honeycomb infill in hollow tubes, documenting significant improvements in crashworthiness metrics characterized by stable and orderly buckling patterns. Technological advancements have yielded significant improvements in structural design, with additive manufacturing (AM) emerging as an increasingly prevalent methodology across diverse engineering applications. The distinctive characteristics of AM-fabricated structures have garnered considerable interest within the researchers.

In one early study, Kucewicz et al. [28] conducted a comparative analysis of conventional and modified honeycomb structures manufactured through fused deposition modeling. Their findings demonstrated that traditional honeycomb configurations exhibited superior energy absorption characteristics compared to their modified counterparts. Building upon this work, Kucewicz et al. [29] expanded their investigation to examine honeycomb structural behavior under varying load conditions. Their results revealed a notable disparity in energy absorption capacity, with specimens under quasi-static loading demonstrating twice the absorption capability of those subjected to dynamic loading conditions. Complementary research by Bates et al. [30] investigated the performance characteristics of graded honeycomb structures produced via fused filament fabrication. Their findings indicated that these structures effectively reduced peak loads, contributing to an overall diminution of structural loading. Further advancing this field, Dar et al. [31] conducted an in-depth analysis of micro-lattice structures under compression, elucidating the critical relationships between cell size, quantity and energy absorption properties.

In recent years, machine learning (ML) has made remarkable advances, with numerous paradigms demonstrating the ability to accurately and effectively predict complex behaviors. Among these contributions, Kumar et al. [32] employed both finite element and ML methods to study the buckling of functionally graded (FG) plates, while Dương et al. [33] utilized artificial neural networks to predict the critical buckling load of such plates, thereby underscoring the efficacy of ML approaches in this domain.

Although the existing literature contains extensive research on the crashworthiness performance of both single and nested tubes, there remains a notable gap in studies that examine the behavioral characteristics of ABS core-filled configurations, particularly in the context of nested and adjoined tubular structures. This research aims to address this gap by conducting a comprehensive evaluation of both ABS core-filled and unfilled shell configurations. The investigation focusses firstly on analysis of the crashworthiness characteristics exhibited by single, nested and adjoined tubes under axial loading in experimental scenario; secondly, the identification of optimal shell configuration through multi-criteria decision-making methodology; and thirdly, an examination of the effects that two distinct ABS core types exert on the crashworthiness of core-filled configurations in simulation. Moreover, this study highlights the benefits of a design that combines materials with contrasting Young's

moduli—specifically, high-modulus steel tubes and low-modulus ABS cores—potentially enhancing crashworthiness through the interaction of these materials. The findings of this study have practical implications for the design of automotive crash boxes, frontal side rails and aerospace impact absorbers, where nested and adjoined tube configurations with enhanced energy absorption and structural stability can address the increasing demand for lightweight, high-performance safety components in modern transportation systems.

2 Methodology

2.1 Indexes estimating the crashworthiness performance

The effectiveness of the crashworthy design features in thin-walled tubes is assessed using several performance metrics: energy absorption (EA), specific energy absorption (SEA), peak crushing load (PCL), mean crushing load (MCL), crushing load ratio (CLR) and structural mass (m). EA, the first index, is calculated using Eq. (1):

$$EA = \int Fdx \tag{1}$$

where F and x denote the crushing load and crushing distance, respectively. SEA, another key index for estimating the effectiveness of the energy-absorbing design, takes into account the material mass (m) and is given by Eq. (2):

$$SEA = \frac{EA}{m} \tag{2}$$

MCL, which is also an essential index for evaluating the effectiveness of the energy-absorbing design, considers the crushing distance (x) and is calculated using Eq. (3):

$$MCL = \frac{EA}{x} \tag{3}$$

PCL, on the other hand, is a critical safety index that is used to predict CLR, as defined by Eq. (4):

$$CLR = \frac{MCL}{PCL} \tag{4}$$

CLR is an important characteristic for assessing the crushing load steadiness of the energy absorber, whereby a higher CLR value indicates superior energy-absorbing stability.

2.2 Entropy evaluation using distance from average solution (EDAS)

Selecting a crashworthy design presents a complex issue due to the conflicting criteria involved. Multi-criteria decision-making (MCDM) techniques are used to determine the optimum design among various alternatives. One effective approach to this challenge is the Evaluation Based on Distance from Average Solution (EDAS) method [34], known for its reliability and computational efficiency. To improve the accuracy of the EDAS method, weighting coefficients are established based on the importance of criteria, utilizing the Entropy method. The Entropy-EDAS approach involves several steps that must be followed:

The weighting coefficient of jth criterion (w_j) is calculated by the Entropy method with following steps:

a) Normalize the decision matrix

$$r_{ij} = \frac{x_{ij}}{\sum_{i=1}^{m} x_{ij}} \tag{5}$$

b) Compute entropy

$$e_j = -h\sum_{i=1}^{m} r_{ij}\ln r_{ij} \quad (j = 1, 2, \ldots, n) \tag{6}$$

where $h = \frac{1}{\ln(m)}$ and m is number of alternatives.

c) Compute the weight vector

$$w_j = \frac{1 - e_j}{\sum_{j=1}^{n}(1 - e_j)} \quad (j = 1, 2, \ldots, n) \tag{7}$$

The ranking of the tubes is determined by using the EDAS method through the following steps:

Step 1: Select the criteria describing alternative.

Step 2: Create the decision matrix where X_{ij} is the evaluation of i^{th} alternative on j^{th} criterion.

$$X = [X_{ij}]_{nxm} \tag{8}$$

Step 3: Determine the average solution (AV_j).

$$AV_j = \frac{\sum_{i=1}^{n} X_{ij}}{n} \tag{9}$$

Step 4: Calculate the positive (PDA) and negative (NDA) distances from average.

$$PDA = [PDA_{ij}]_{nxm} \tag{10}$$

$$NDA = [NDA_{ij}]_{nxm} \tag{11}$$

a) In case of j[th] beneficial criterion

$$PDA_{ij} = \frac{max\,(0, (X_{ij} - AV_j))}{AV_j} \tag{12}$$

$$NDA_{ij} = \frac{max\,(0, (AV_j - X_{ij}))}{AV_j} \tag{13}$$

b) In case of j[th] non-beneficial criterion

$$PDA_{ij} = \frac{max\,(0, (AV_j - X_{ij}))}{AV_j} \tag{14}$$

$$NDA_{ij} = \frac{max\,(0, (X_{ij} - AV_j))}{AV_j} \tag{15}$$

Step 5: Calculate the weighted sum of PDA and NDA for all alternatives where w_j is the weighting coefficient of j[th] criterion.

$$SP_i = \sum_{j=1}^{m} w_j PDA_{ij} \tag{16}$$

$$SN_i = \sum_{j=1}^{m} w_j NDA_{ij} \tag{17}$$

Step 6: Normalize the SP and SN for all alternatives.

$$NSP_i = \frac{SP_i}{max_i\,(SP_i)} \tag{18}$$

$$NSN_i = 1 - \frac{SN_i}{max_i\,(SN_i)} \tag{19}$$

Step 7: Calculate the appraisal score (AS) for all alternatives and find the rank where $0 \leq AS_i \leq 1$.

The Entropy–EDAS procedure (Fig. 1) follows three stages: (i) normalization and entropy-based weighting of criteria, (ii) computation of positive/negative distances from the average solution (PDA/NDA) for beneficial and non-beneficial criteria and (iii) weighted aggregation, normalization and computation of the appraisal score (AS) used to rank alternatives. This hybrid procedure preserves objective weighting while providing an intuitive distance-based ranking that balances benefit and risk.

2.3 Sample preparation, experiment setup and material properties

To investigate the influence of tube arrangement on crashworthiness performance under axial compression, this study

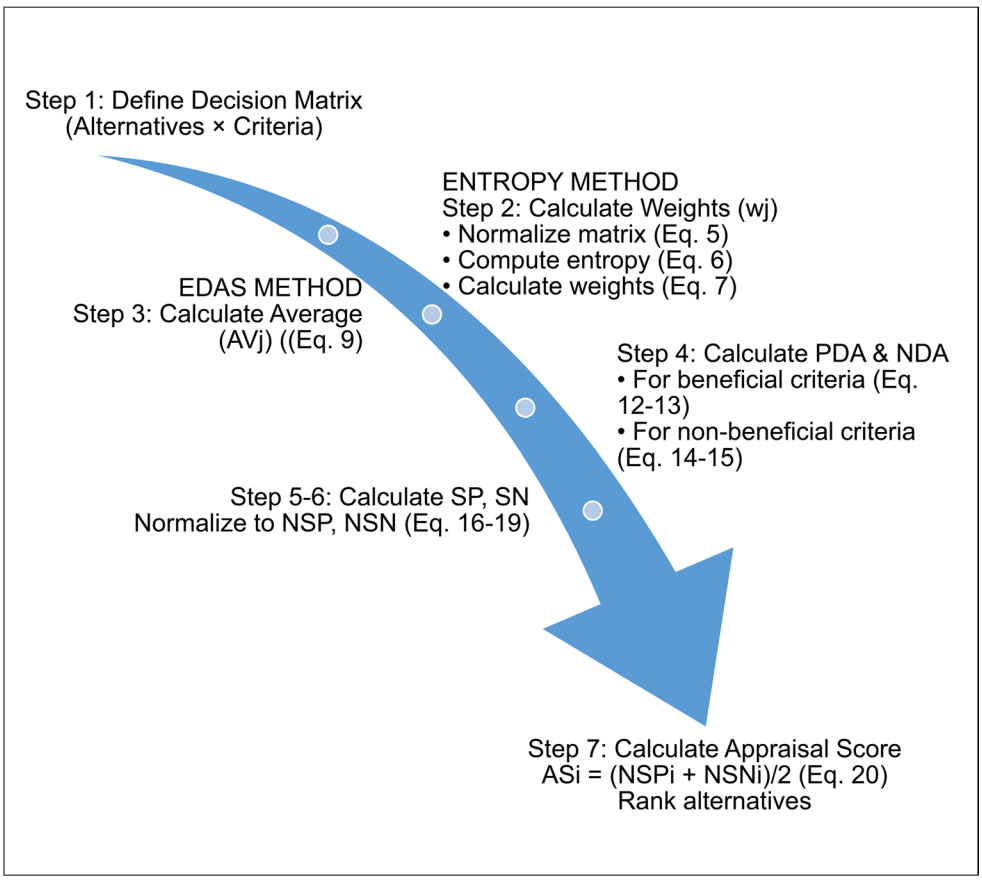

Fig. 1 Flowchart of the Entropy-EDAS method

proposes three distinct configurations: nested, single and adjoined tubes. The samples examined were fabricated from component tubes, each measuring 200 mm in length and cut from commercially available CT3 mild steel tubes (Fig. 2(a)). These component tubes featured both rectangular and square cross-sections, with dimensions of 40×80, 50×100, 60×120, 60×60, 70×70 and 90×90 mm². The wall thicknesses of the tubes were standardized at 1.2 and 1.3 mm.

As depicted in Fig. 2(b), nested tubes consist of two tubes joined together, utilizing rectangular tubes with dimensions of 50×100 mm² and 60×120 mm², as well as square tubes measuring 60×60 mm², 70×70 mm² and 90×90 mm². Single tubes, in contrast, are composed of either a rectangular tube measuring 60×120 mm² or a square tube measuring 90×90 mm². Adjoined tubes employ two rectangular tubes with dimensions of 40×80 mm² and are characterized by two distinct configurations: the component tubes can be arranged either parallel or perpendicular to one another. Cyanoacrylate adhesive was utilized to secure the component tubes in the adjoined tube configuration, enabling them to remain in place before testing.

To facilitate efficient sample identification and analysis, each sample was assigned a unique code as shown in Table 1. Specifically, NRT, NST, SingleT, and ART denote nested rectangular, nested square, single and adjoined rectangular tubes, respectively. Notably, all tubes within nested and single configurations have a wall thickness of 1.3 mm, with the exception of the adjoined tube which has a thickness of 1.2 mm. For core-filled samples analyzed by finite element analysis, NST2(FEA)_C2 corresponds to the second nested square tube filled with core type 2 of 1 mm thickness (Fig. 8).

The experimental phase of this study involved conducting compression tests utilizing a 500 kN testing apparatus, as illustrated in Fig. 2(c). Prior to the initiation of each test, individual specimens were carefully positioned between the upper platen and lower table of the machine, ensuring proper alignment for axial loading. In accordance with the methodology employed by Tabacu and Ducu [35], the tests were conducted at a constant velocity of 5 mm/min. The compression process continued until the specimen reached a state of densification, defined by Wang et al. [36] as compression to two-thirds of the tube's initial length. Throughout the crushing process, the testing apparatus automatically recorded force-displacement data and the tube's deformations during the test were captured using a camera. This approach to data collection, combining force-displacement measurement with structural deformation, facilitates a more nuanced understanding of the sample's behavior under axial compression.

Figure 3 presents the stress-strain curves and mechanical properties of both the CT3 mild steel and ABS materials used in this study. The ABS material exhibited the following characteristics: a density of 1.02 g/cm³, a Poisson's ratio of 0.33, a Young's modulus of 1.1 GPa and an initial yield

Fig. 2 (**a**) Tube cutting, (**b**) Tube arrangement and (**c**) Testing apparatus

Table 1. Tubes with abbreviations and parameters

Code	Component tube			t (mm)	L (mm)	Feature
	Inner tube axb (mm)	Outer tube	t (mm)			
NRT(SPL1)	50 × 100	60 × 120	1.3	-	200	Bi-tubular nested tube
NST1(SPL1)	60 × 60	70 × 70				
NST2(SPL1)	60 × 60	90 × 90				
NST3(SPL1)	70 × 70	90 × 90				
SingleT-9 × 9	90 × 90					Single tube
SingleT-6 × 12	60 × 120					
ART1(SPL1)	40 × 80	40 × 80	1.2			Parallel tube
ART2(SPL1)						Perpendicular tube
NRT(FEA)_C1	50 × 100	60 × 120	1.3	1		C1 core-filled tube
NRT(FEA)_C2						C2 core-filled tube
NST1(FEA)_C1	60 × 60	70 × 70				C1 core-filled tube
NST1(FEA)_C2						C2 core-filled tube
NST2(FEA)_C1	60 × 60	90 × 90				C1 core-filled tube
NST2(FEA)_C2						C2 core-filled tube
NST3(FEA)_C1	70 × 70	90 × 90				C1 core-filled tube
NST3(FEA)_C2						C2 core-filled tube
ART1(FEA)_C1	40 × 80	40 × 80	1.2			C1 core-filled tube
ART1(FEA)_C2						C2 core-filled tube
ART2(FEA)_C1						C1 core-filled tube
ART2(FEA)_C2						C2 core-filled tube

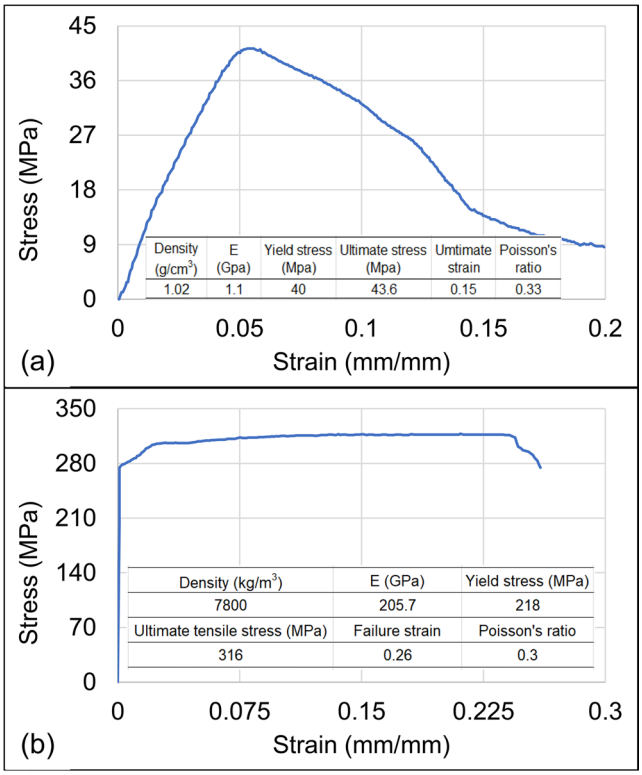

Fig. 3 Stress-strain curves and mechanical characteristics of: (**a**) ABS and (**b**) CT3 mild steel

strength of 40 MPa. In contrast, the CT3 mild steel demonstrated a density of 7.8 g/cm³, a Poisson's ratio of 0.3, a Young's modulus of 205.7 GPa and an initial yield strength of 218 MPa. Combining these two materials has potential applications in the field of crashworthiness, leveraging the lightweight and flexible nature of ABS with the strength and rigidity of CT3 mild steel.

2.4 Machine learning

Random forest algorithm [37], a machine learning paradigm, augments the robustness and accuracy of predictions by combining multiple models' outputs, while demonstrating remarkable versatility in both classification and regression applications. Given the inherent complexity of the data, this paradigm was then applied to estimate the load, as illustrated in Fig. 4, which presents the random forest's tree-based prediction methodology.

To assess the validity of the model, the following performance criteria are defined:

- Accuracy is determined using Eq. (21):

$$Accuracy\ (\%) = \left(1 - \sum \frac{|y_i - \widehat{y}_i|}{|y_i|}\right) \times 100 \qquad (21)$$

where y_i and $\widehat{y}_i$ represent the actual and predicted values, respectively.

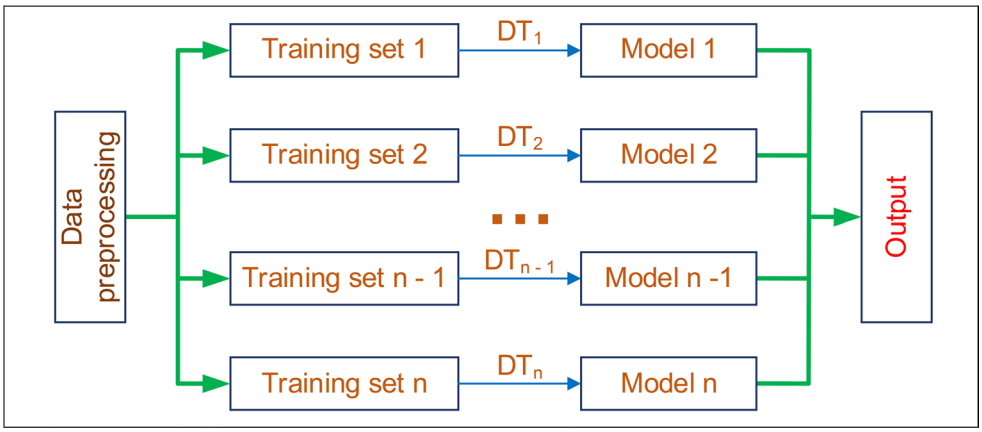

Fig. 4 Random forest

- The coefficient of variation (R^2) is calculated using Eq. (22):

$$R^2 = 1 - \frac{\sum (y_i - \widehat{y}_i)^2}{\sum \left(y_i - \bar{y}\right)^2} \tag{22}$$

where $\bar{y}$ is the mean of the actual values.

- The root-mean-square error (RMSE (%)) is computed as per Eq. (23):

$$RMSE\,(\%) = \left(\sqrt{\frac{\sum_{i=1}^{N}\left(y_i - \widehat{y}_i\right)^2}{N}} \Big/ \bar{y}\right) \times 100 \tag{23}$$

Although higher values of accuracy and R^2 generally indicate superior performance, it should be noted that when accuracy approaches 100 and R^2 nears 1, such results are not necessarily preferred as they may indicate overfitting—a significant concern in machine learning applications. Table 2 presents the performance criteria with acceptable values for both non-core and core filled tubes, thereby validating the model's accuracy through these carefully calibrated metrics.

Table 2 Prediction capability

Data	Accuracy (%)	R^2	RMSE (%)
NRT	92.83	0.8889	5.42
NST1	91.53	0.8627	5.94
NST2	90.75	0.8518	5.79
NST3	91.18	0.8659	5.63
ART1	90.27	0.8201	5.76
ART2	91.22	0.8351	4.98
C1	91.39	0.9578	4.25
C2	90.55	0.9337	5.21
HFT	93.57	0.8849	4.64

2.5 Finite element (FE) model and mesh convergence study

In this investigation, FE models, developed using the LS-DYNA solver, were employed to examine the behavior of mild steel tubes cored with Acrylonitrile Butadiene Styrene (ABS), with model accuracy assessed through comparative analysis of numerical outcomes against experimental results. These simulations not only elucidated the deformations of both nested and adjoined tubes with cores but also demonstrated the beneficial effects of core integration in enhancing crashworthiness. Belytschko-Tsay 4-node shell elements were adopted for modeling the walls, while rigid platens with an unrefined mesh were employed for compression. Material behavior was characterized using the MAT024 model, with properties delineated in Fig. 3, accounting for the strain-rate sensitivity of both mild steel [38] and ABS [39] to accurately capture the strain-rate effects on material strength. The lower platen, capable of axial movement in the z-direction, contrasted with the upper platen, which remained stationary. The 'contact-automatic-surface-to-surface' and 'contact-automatic-single-surface cards' were utilized to simulate tube-platen interaction and tube self-contact during folding.

In simulation, mesh size selection is a critical issue due to its significant effect on crashworthiness indices and computational cost. A mesh convergence analysis was therefore performed using five mesh sizes: 1.5 mm, 2 mm, 3 mm, 4 mm and 5 mm. The load responses for these mesh sizes are displayed in Fig. 6, which shows that the load responses of 1.5 mm, 2 mm and 5 mm are similar to each other, while the load responses of 3 mm and 4 mm mesh sizes differ from those of 1.5 mm, 2 mm and 5 mm. Observation of Fig. 5 reveals that with increasing mesh size, PCLs gradually decrease, whereas EAs initially increase and subsequently decrease. Additionally, the differences in EA and PCL between 1.5 mm and 2 mm are 0.61% and 3.94%, respectively, while the differences in EA and PCL for the remaining mesh sizes compared with the 1.5 mm mesh size range from 4.25% to 9.9%.

Mesh size (mm)	EA (kJ)	Diff. (%)	PCL (KN)	Diff. (%)
1.5	6.22	-	163.14	-
2	6.26	0.61	156.71	-3.94
3	6.76	8.70	151.53	-7.11
4	6.77	8.75	150.47	-7.77
5	6.48	4.25	146.99	-9.90

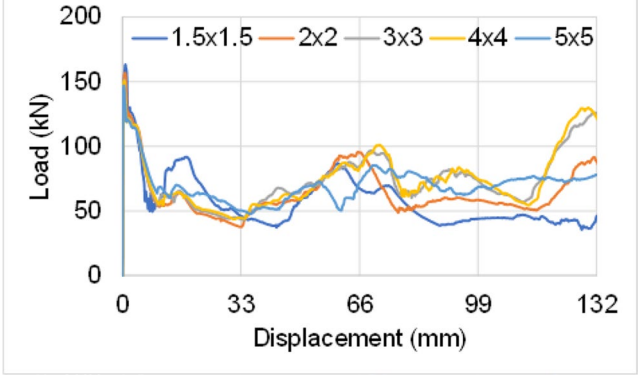

Fig. 5 Mesh convergence analysis

Therefore, considering both the accuracy and efficiency of the simulation, a mesh size of 2 mm was selected as the optimal size for numerical simulation.

2.6 Validation

To establish the credibility of the numerical simulation, we compared results from numerical simulations, experimental tests and machine learning outcomes. Numerical simulations, depicted in Fig. 6 for non-filled tubes and Fig. 7 for ABS cores and core-filled tubes, were performed to validate the FE models by replicating the experimental tests conducted. Figure 6 presents the load-displacement curves, peak crushing loads (PCLs), mean crushing loads (MCLs) and deformation modes for nested and joined tubes. Both the deformation patterns and load responses show excellent agreement between simulations and tests, with average differences in MCLs and PCLs of only 3.12% and 3.57%, respectively.

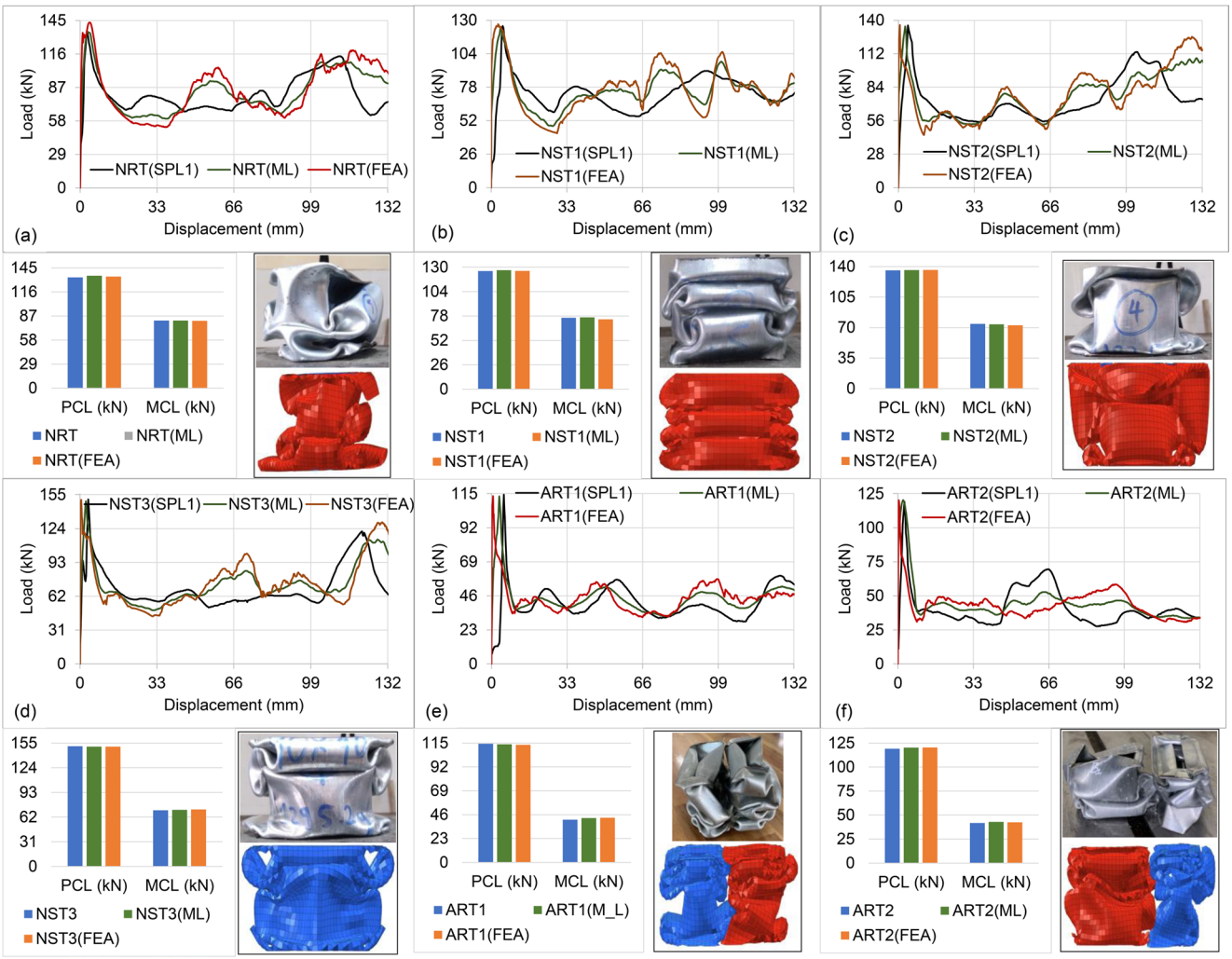

Fig. 6 Validation of non-core-filled tubes: (**a**) NRT, (**b**) NST1, (**c**) NST2, (**d**) NST3, (**e**) ART1 and (**f**) ART2

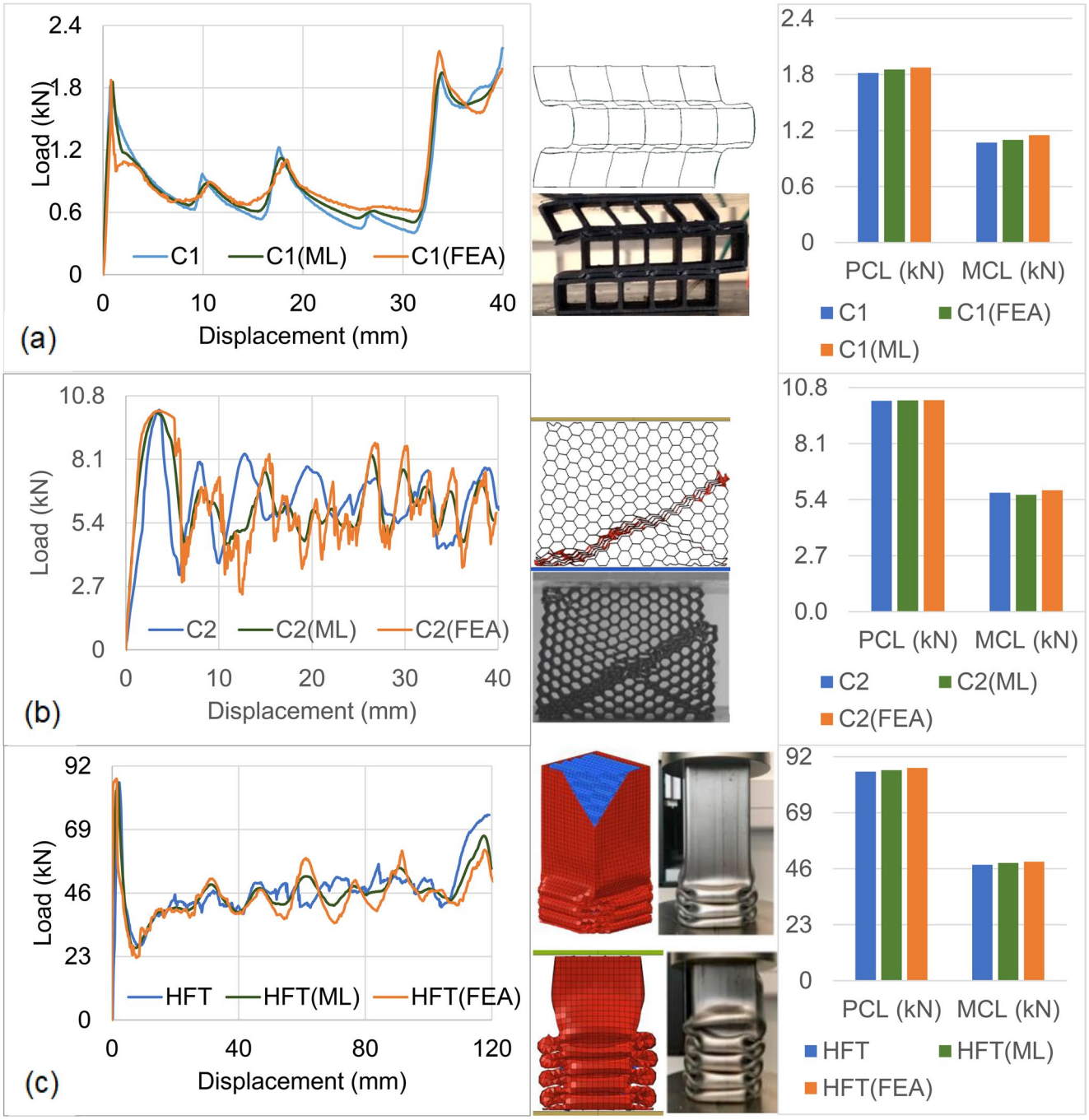

Fig. 7 Validation of cores and core filled tube: (**a**) Core 1 [40], (**b**) Core 2 [28] and (**c**) Honeycomb filled tube [41]

Figures 7(a and b) display the load curves, deformation responses and comparisons of PCL and MCL for the ABS_C1 core [40] and ABS_C2 core [28], respectively, exhibiting near-perfect agreement with experimental results. This close alignment between numerical and experimental outcomes validates the accuracy of the models for ABS cores. To further substantiate the FE model's reliability, a comparison of crushing behavior and load response for a honeycomb-filled tube is provided in Fig. 7(c), referencing the experimental test reported in [41]. Notably, the numerical and experimental deformation modes align well. The load responses derived from both experiments and simulations exhibit consistent patterns, corresponding to the folding positions. Moreover, the loads obtained from experiments and simulations of three samples closely match for the PCLs and MCLs, with approximate discrepancies of 3.2%, 0.27%, and 1.71%, respectively.

Moreover, the comparisons between numerical simulation and machine learning methodologies, as presented in both Figs.

6 and 7, reveal that the loads collected from simulations and the machine learning paradigm of all samples closely match for the PCLs and MCLs, with acceptable divergences ranging from 1.82% to 3.45%. Consequently, the FE method is sufficiently accurate for simulating the process in subsequent sections.

Based on the validations above, a further investigation of the tube arrangement and core on crashworthiness performance was performed. FE models were accordingly developed for both the standard tubes and their ABS-filled counterparts, as illustrated in Fig. 8.

3 Results and discussion

3.1 Deformation, load and energy absorption of unfilled samples

To investigate the crashworthiness characteristics of the samples, a series of nine experiments were conducted across three groups: nested, single and adjoined. Then, the experimental results underwent analysis, with a particular focus on the deformation behavior and load response of the samples. The deformation, load and energy absorption characteristics of nested, single and adjoined tubular structures, as depicted in Figs. 9, 10 and 11, demonstrate distinct load fluctuation patterns corresponding to the progressive development of structural folds. During experimental testing, the observed irregularities in deformation modes can be attributed to two interconnected factors: the manual cutting process, which resulted in imperfect box-shaped tubes characterized by low cutting quality due to tolerance issues such as uneven edges and dimensional variations and the dimensional inconsistencies, wherein one side slightly exceeded the length of its opposite face, thereby inducing imperfect deformation patterns during compression testing. The formation of plastic hinges within the folds occurred at arbitrary locations, primarily influenced by the compression resistance of the constituent tube. As the lower table ascended, the majority of the samples underwent plastic deformation under compression, ultimately resulting in failure without buckling collapse. In the final stages of the compression process, densification occurred, leading to an increase in both compressive load and energy absorption.

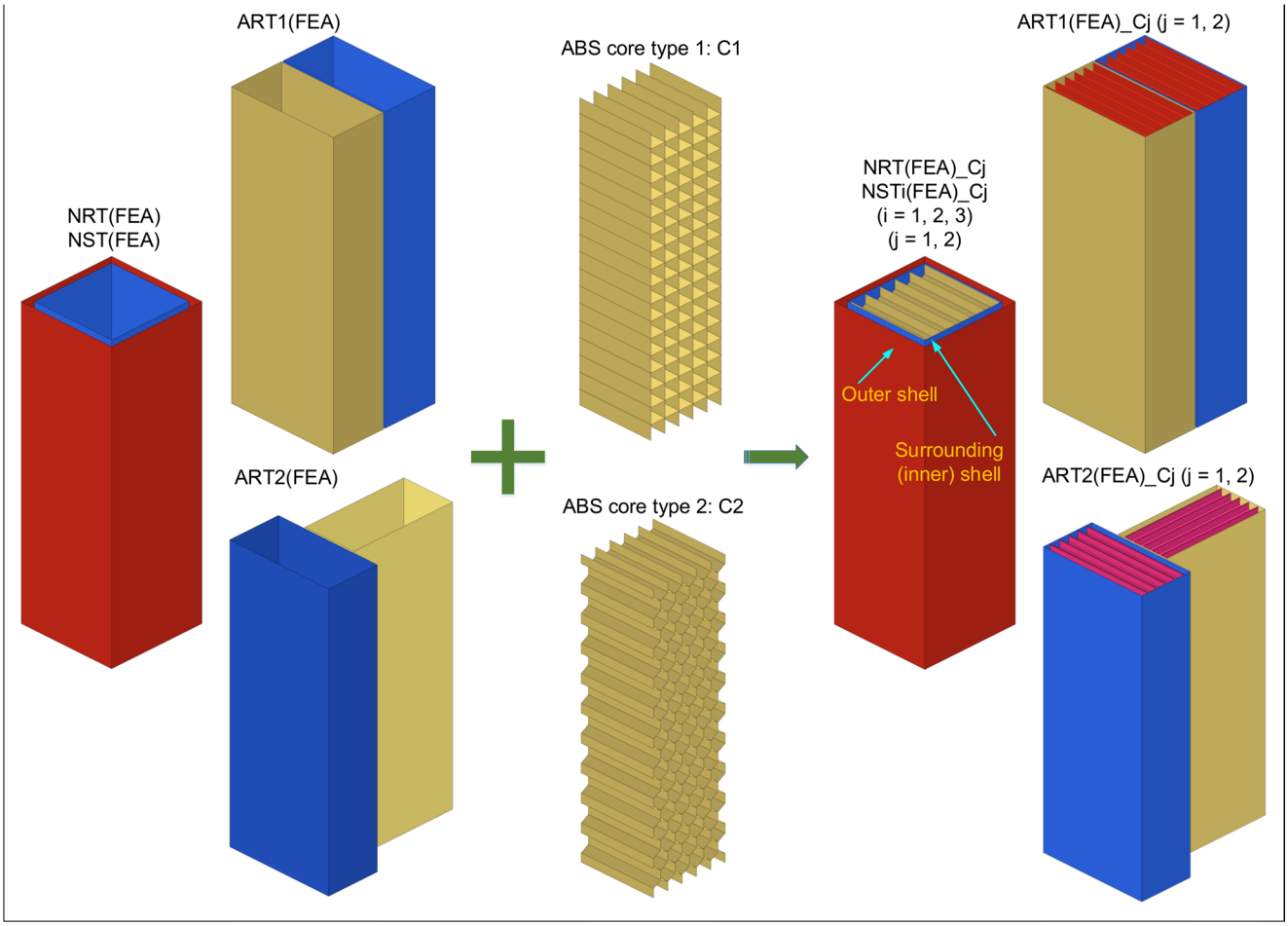

Fig. 8 Core-filled tubes

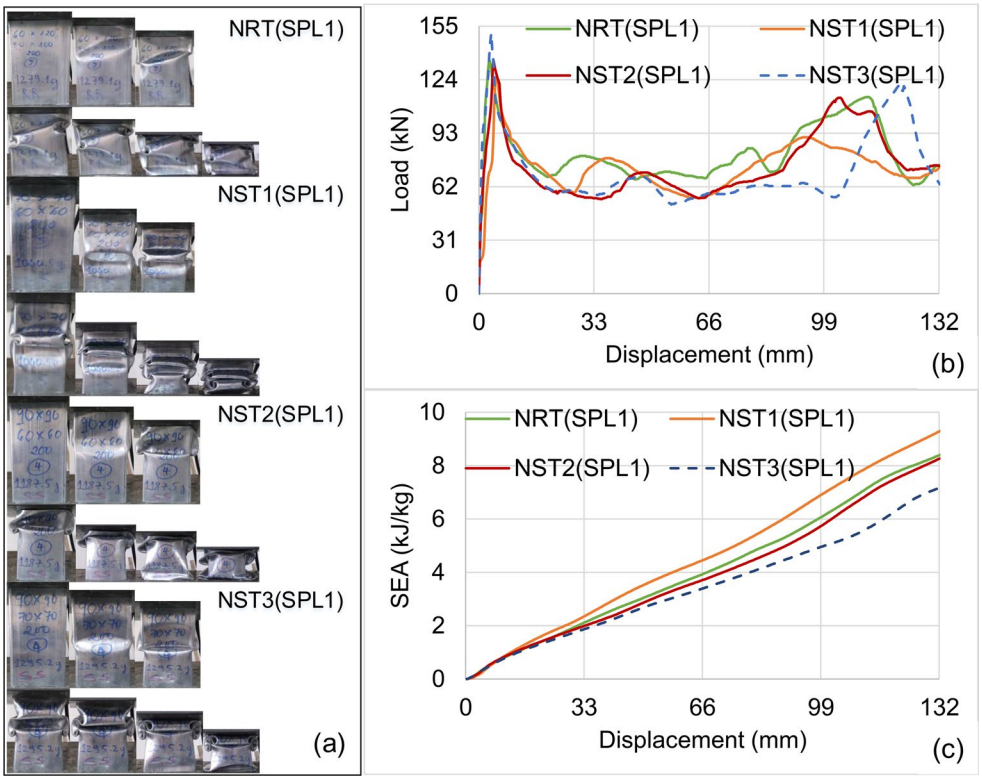

Fig. 9 NRT and NST samples: (**a**) Deformation, (**b**) Load and (**c**) SEA responses

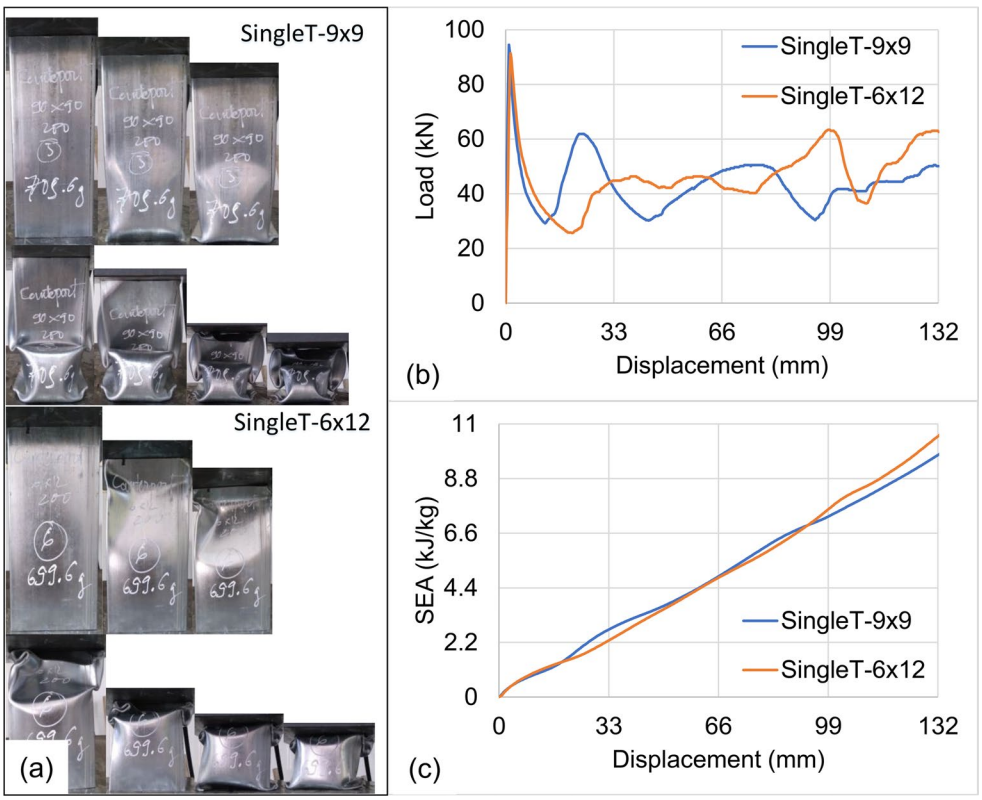

Fig. 10 Single tubes: (**a**) Deformation, (**b**) Load and (**c**) SEA responses

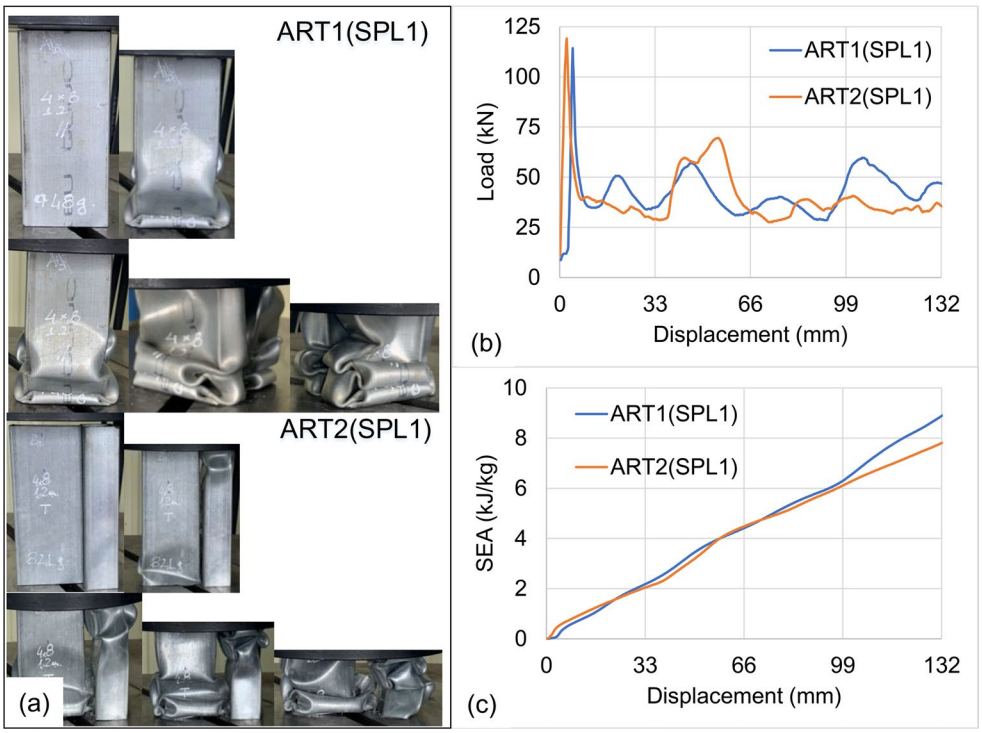

Fig. 11 ART samples: (**a**) Deformation, (**b**) Load and (**c**) SEA responses

3.1.1 Nested samples (NRT and NST)

As shown in Fig. 9(a), the nested specimens exhibited plastic hinges at varying positions along their lengths, resulting in different deformation modes [42]. This variation can be attributed to the specimens' differing crushing resistances. For instance, the NRT(SPL1) and NST2(SPL1) samples developed plastic hinges near their upper ends, whereas the NST1(SPL1) and NST3(SPL1) samples exhibited plastic hinges forming in the middle. Consequently, there was no consistent deformation mode among the nested samples.

Although all three experimental specimens—NRT(SPL1), NST2(SPL1) and NST3(SPL1)—demonstrated characteristic inward bending of their tube walls, detailed analysis revealed slight differences in their final deformation patterns. In the case of NST2(SPL1), during the later stage of deformation, deformations formed at the upper and lower ends, however a large undeformed region persisted in the middle of the outer tube. Similarly, in the NRT(SPL1) sample, both the upper and lower ends exhibited deformation; however, the undeformed region in the middle was smaller than that of NST2(SPL1). The deformation pattern in the NST3(SPL1) sample mirrored that of NST2(SPL1), with the deformation of the inner tube preventing the formation of a middle fold in the outer tube, resulting in an incomplete fold in this region. This similarity highlights the inner tube's resistance to the overall deformation of the structure.

The majority of the examined specimens exhibited non-repeating fold patterns; a phenomenon primarily attributed to inadequate constraint between the constituent tubes during preparation. Under compressive loading, the interaction between the inner and outer walls causes the inner tube to skew, resulting in erratic deformation without consistent fold patterns. Consequently, the deformation and energy absorption characteristics of the outer tube are significantly influenced by the deformation of the inner tube, which in turn affects the overall deformation mode of the specimen [43]. In contrast, the NST1(SPL1) sample demonstrated a deformation characterized by repetitive folds, indicating simultaneous deformation of both component tubes; a configuration generally considered optimal for energy absorption [44].

The load-displacement curves in Fig. 9(b) illuminated the failure processes of the NRT and NST specimens, which, while initially similar, exhibited significant divergence in the mid- and late-stages due to distinct crushing behaviors. The NRT(SPL1) sample stood out with a notably higher load, indicating superior anti-crushing and energy absorption capabilities. The NST3(SPL1) sample had the largest PCL, with others being quite comparable. In the early compression stage, the compressive load of the NST3(SPL1) sample reached its peak sooner than the others, likely due to the earlier formation of plastic hinges, contributing to its higher stiffness. The PCL was then attained at different times, depending on the compression strength and constituent tubes of each sample.

Compared to the other samples, the NST1(SPL1) sample displayed smoother load fluctuations, resulting in repeated folds, while the remaining samples exhibited significant

load fluctuations during the middle and later stages of the compression process. In the case of the remaining samples, the deformation of the inner tube generated a stiffening effect on the sample. Consequently, the load fluctuation reflects the collapsing modes of the samples. During compressive loading, the energy absorption mechanism is predominantly governed by plastic deformation processes, wherein substantial energy expenditure is required for the formation of plastic hinges [45]. Subsequently, the mass-dependent energy absorption characteristic of the nested group was evaluated through an analysis of SEA, underscoring the significance of SEA as a critical performance indicator of energy absorption efficiency, particularly during the late stage of deformation. As illustrated in Fig. 9(c), during the later stages of compression, the SEAs of samples NST1(SPL1) and NST3(SPL1) exhibit the largest and smallest values, respectively, compared to other samples. This variation is primarily attributable to their corresponding smallest and largest masses. Therefore, it is imperative to consider structural mass when assessing a sample's SEA.

3.1.2 Single samples (SingleT)

Figure 10 highlights the distinctive differences in deformation, load and SEA responses between the SingleT-9 × 9 and SingleT-6 × 12 samples, where the initial formation of plastic hinges played a crucial role in determining their failure modes. In the SingleT-9 × 9 sample, plastic hinges at the lower end triggered the development of two large folds, whereas in the SingleT-6 × 12 sample, plastic hinges at both ends led to localized bulging in the middle and smaller folds at the upper and lower corners. Consequently, the distinct tube profiles and initial plastic hinge locations resulted in divergent deformation modes for the two samples.

The load-displacement behaviors of the SingleT-9 × 9 and SingleT-6 × 12 samples, depicted in Fig. 10(b), initially exhibit similar load profiles; however, their behavior during collapse reveals contrasting anti-compressing and energy absorption capabilities. Despite having a lower PCL, the SingleT-6 × 12 sample significantly outperforms the SingleT-9 × 9 in the later stages of compression, sustaining a higher load level and demonstrating superior energy absorption. This enhanced performance aligns with the SEA responses shown in Fig. 10(c), where the SingleT-6 × 12 sample consistently attains a higher SEA value from a crushing distance of 115 mm onwards. This behavior is attributed to the increased densification and compressive strength observed at the corners of the SingleT-6 × 12, in contrast to the lower level of densification and compressive strength observed at the corners of the SingleT-9 × 9, which are critically important regions for dissipating crushing energy and regulating overall energy absorption capacity [46].

3.1.3 Adjoined samples (ART1 and ART2)

Differing from the nested configurations, the tested samples comprised two adjoined tubes arranged in either parallel (ART1(SPL1)) or perpendicular (ART2(SPL1)) configurations (Fig. 11(a)). The resulting failure locations and deformation modes significantly differed between these arrangements due to variations in the tube's crushing resistance. In ART1(SPL1) sample, concurrent failures at the lower ends of both tubes led to concentrated folds in those regions. Conversely, in ART2(SPL1) sample, diverse plastic hinges across two component tubes yielded folds at both upper and lower ends, resulting in distinct deformation patterns and energy absorption characteristics. Notably, mutual warping of the interacting tubes under compression, as observed in Fig. 11(a), reduced the material undergoing plastic collapse and consequently decreased energy absorption. Therefore, the specific failure mechanisms play a crucial role in determining the energy absorption capacities of these adjoined configurations.

Analyzing load and SEA responses in Figs. 11(b)-(c) reveals contrasting deformation behaviors for ART1(SPL1) and ART2(SPL1) samples. Despite a lower PCL than ART2(SPL1), ART1(SPL1) exhibits a consistently higher load level during the later compression sta

ge (Fig. 11(b)). This discrepancy can be attributed to the difference in tube arrangement. The parallel configuration of ART1(SPL1) likely allows for greater material engagement during later stages, contributing to its sustained load. Conversely, ART2(SPL1)'s perpendicular arrangement leads to an earlier PCL, however subsequent bending of its component tubes results in a decrease in load and, consequently, SEA (Fig. 11(c)). This suggests that the parallel arrangement in ART1(SPL1) provides superior anti-crushing and energy absorption capacity during the later stages of compression, despite its lower initial peak load.

3.2 Difference in crashworthiness performance

Achieving high-performance crashworthy designs requires maximizing the SEA while minimizing the PCL and mass [47]. This balance demands efficient energy absorption mechanisms capable of dissipating a large amount of energy per unit mass within an acceptable PCL range. In this section, the crashworthiness performance of various configurations (Fig. 2) is compared using indices evaluated at a displacement of 132 mm during compression. This displacement corresponds to approximately two-thirds of the tube's initial length (200 mm), representing the effective crushing distance commonly adopted in axial compression studies [36, 48]. Following the procedures reported in these works, the compression stroke was limited to two-thirds of the initial

Fig. 12 Difference in deformation of constituent tubes: (**a**) Nested tube and (**b**) Adjoined tube

tube length to ensure that all crashworthiness indices were assessed within the stable progressive folding stage—prior to the onset of densification, where fold compaction leads to a rapid load increase and diminished energy absorption efficiency. Therefore, 132 mm was selected as the effective crushing displacement for consistent and meaningful comparison across all configurations.

Analysis of the crushing mechanisms in Figs. 9, 10 and 11 reveals two primary collapse modes: irregular folding and repeated folding. This finding highlights a clear link between the geometric arrangement of tubes and their collapse behavior. Interestingly, repeated folding deformation predominantly occurred in nested and adjoined samples featuring a small gap between component tubes, as well as in SingleT-9×9 samples. This pattern underscores the pivotal role of tube interaction in determining the energy absorption mode. Notably, as illustrated in Fig. 12, the interaction between component tubes in nested and adjoined configurations significantly influences their deformation. In nested samples, the failure mode of the outer tube often dictates the failure mode of the inner tube, demonstrating a more pronounced influence of tube interaction compared to adjoined samples.

Table 3 reveals a direct correlation between MCL and EA, consistent with findings reported by Schneider and Jones [49]. For example, the NRT(SPL1) sample exhibits the highest EA, its SEA may not be as efficient compared to other configurations. This highlights the importance of considering multiple crashworthiness indices beyond axial crushing characteristics. PCL, MCL, CLR and SEA offer deeper insights for robust comparison and evaluation, as presented in Fig. 13.

Figure 13(a) presents a comparison of PCL across sample configurations. Among nested samples, NST3(SPL1) stands out with a PCL of 16.77% higher than its peers due to the simultaneous loading of both large-diameter tubes. This observation underscores a clear proportionality between PCL and component tube parameters in nested samples, with larger dimensions contributing to higher loads. In contrast, SingleT and adjoined samples exhibit relatively consistent PCLs, averaging 62% and 29% lower, respectively, than NST3(SPL1). This discrepancy reflects the influence of the number of loaded tubes, with single-tube configurations in SingleT samples minimizing PCL.

In Fig. 13(b), a comprehensive analysis of MCL across all samples is presented. Within the nested samples, a gradual decline in MCL is observed from the NRT(SPL1) sample to the NST3(SPL1) sample. Specifically, the NRT(SPL1) sample attains the highest MCL, whereas the NST3(SPL1) sample, characterized by a larger gap between its two component tubes, exhibits the smaller MCL. MCLs for the SingleT and ART samples demonstrate comparable values. Notably, the average MCL for nested samples is approximately 69.8% and 85.55% greater than those for SingleT and ART samples, respectively. This figure underscores a significant distinction between nested samples and the remaining set, highlighting the considerable impact of both tube arrangement and tube parameters on MCL.

In Fig. 13(c), a consistent pattern in Crush Load Ratios (CLRs) is discernible, with nested samples exhibiting higher CLR values compared to SingleT and ART samples. Overall, CLR exhibits a gradual decrease from the NRT(SPL1) sample to the ART2(SPL1) sample. The NRT samples, in particular, show a noteworthy increase in CLR attributed to the pronounced interaction between their two component tubes. In contrast, the ART1 and ART2 samples demonstrate a reduction in CLR due to a weaker interaction and the absence of constraint between the two component tubes. Accordingly, the average CLR for the nested samples is approximately

Table 3 Main indexes of all the samples

Code	m (kg)	PCL (kN)	MCL (kN)	CLR	SEA (kJ/kg)	EA (kJ)
NRT(SPL1)	1.279	129.86	83.02	0.64	8.27	10.58
NST1(SPL1)	1.041	125.64	75.99	0.60	9.14	9.51
NST2(SPL1)	1.188	135.69	74.61	0.55	8.12	9.65
NST3(SPL1)	1.295	150.94	71.66	0.47	7.06	9.14
SingleT-9×9	0.710	94.48	43.59	0.46	7.90	5.60
SingleT-6×12	0.700	91.33	46.30	0.51	8.34	5.83
ART1(SPL1)	0.748	114.27	41.87	0.37	7.16	5.36
ART2(SPL1)	0.821	119.09	40.39	0.34	6.64	5.45

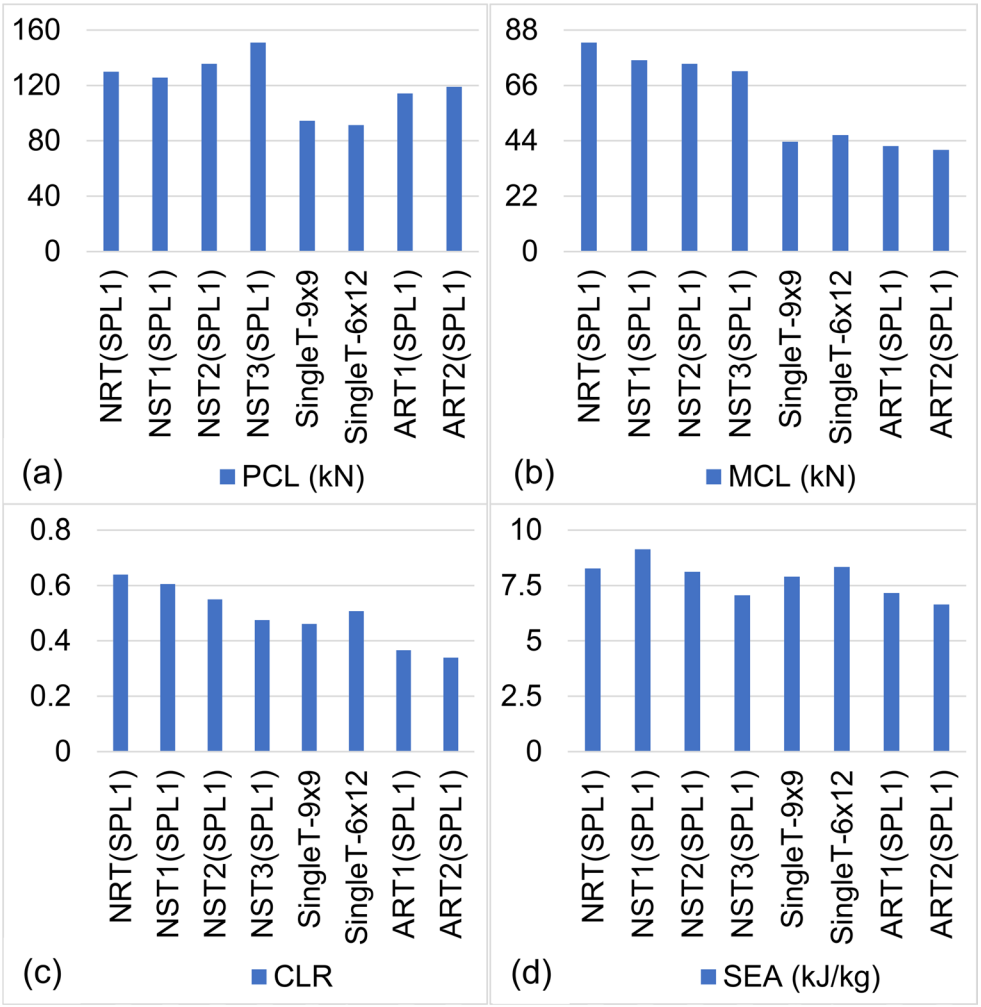

Fig. 13 Difference in (**a**) PCL, (**b**) MCL, (**c**) CLR and (**d**) SEA

17.14% and 60.77% higher than those obtained for the SingleT and ART samples, respectively. These observations underscore the pivotal role of interaction and constraint of the component tubes in improving the MCL.

Figure 13(d) compares SEA across all samples, revealing differences in their SEA. Notably, NST1(SPL1) and ART2(SPL1) exhibit the highest and lowest SEA, respectively. This disparity in ART2(SPL1)'s SEA stems from the weak interaction of its component tubes, requiring less crushing load and energy to form folds. Meanwhile, ART1(SPL1)'s SEA exceeds both ART2(SPL1) and NST3(SPL1) due to its stronger crushing resistance compared to ART2(SPL1) and its lower mass compared to NST3(SPL1). Generally, adjoined samples display lower energy absorption efficiency than nested samples owing to their weaker tube interaction. However, sample mass plays a crucial role in determining SEA. For instance, while ART1(SPL1)'s energy absorption is 49% lower than NRT(SPL1), its SEA is 13% smaller due to its lower mass. These findings underscore the critical influence of tube arrangement, cross-section and mass on the crashworthiness performance of the examined samples.

3.3 Optimum structure for crashworthiness application

While Sect. 3.2 provided a comparison of crashworthiness performance, considering factors such as mass, geometric configurations and tube arrangement, it did not conclusively identify an optimal structure for crashworthiness applications. Identifying the most suitable architecture for crashworthiness remains a challenging task. To address this challenge, we apply the Entropy-EDAS decision-making method to determine the most efficient architecture for crashworthiness design.

Effective energy absorption is crucial for structures designed to ensure occupant safety, traditionally assessed using the CLR, EA and SEA indices. These indices quantify the absorbed energy relative to the structure's mass, emphasizing the importance of mass minimization for fuel efficiency. However, high PCL or deceleration during impact scenarios can significantly increase injury risk. Therefore, minimizing the PCL index and maintaining it within a safe range becomes paramount for harm prevention.

Consequently, mass and PCL represent "non-beneficial" criteria, while CLR, EA and SEA are deemed "beneficial" for crashworthiness design.

The weighting coefficients for the aforementioned indices, determined using the Entropy method as calculated by Eqs. 5–7 and presented in Table 4, were subsequently utilized in the EDAS method. The results of steps 1–6 of the EDAS method are summarized in Tables 5, 6, 7, and 8. Table 9 presents the appraisal scores (AS) and corresponding sample rankings, ultimately identifying the NST1 sample, which has the highest AS value, as exhibiting the optimal shell architecture based on the established crashworthiness criteria.

In the realm of crashworthiness design, PCL plays a crucial role in ensuring passenger safety, with its value thresholds typically constrained within specific ranges that are dependent on the type of vehicle under consideration. This importance is exemplified in the work of Chen et al. [50], who, in their crashworthiness optimization study for multi-cell tubes, applied a PCL constraint of 100 kN. Building upon this research, Yin et al. [51] conducted an exploration to identify an optimal structure for crashworthiness applications, employing a more expansive PCL range of 119 kN to 158 kN, which further underscores the variability in PCL thresholds across different studies and vehicle types.

Table 4 Normalized decision matrix and weighting coefficients (w_j)

Code	Normalized decision matrix				
	m	PCL	CLR	SEA	EA
NRT(SPL1)	0.16	0.14	0.16	0.13	0.17
NST1(SPL1)	0.13	0.13	0.15	0.15	0.16
NST2(SPL1)	0.15	0.14	0.14	0.13	0.16
NST3(SPL1)	0.17	0.16	0.12	0.11	0.15
SingleT-9 × 9	0.09	0.10	0.12	0.13	0.09
SingleT-6 × 12	0.09	0.10	0.13	0.13	0.10
ART1(SPL1)	0.10	0.12	0.09	0.11	0.09
ART2(SPL1)	0.11	0.12	0.09	0.11	0.09
Entropy (e)	0.985	0.994	0.990	0.998	0.981
wj	0.29	0.12	0.19	0.05	0.36

Table 5 Decision matrix and their weighting coefficients

w_j	Non Benf.	Non Benf.	Benf.	Benf.	Benf.
	0.287	0.117	0.189	0.045	0.362
Code	m (kg)	PCL (kN)	CLR	SEA (kJ/kg)	EA (kJ)
NRT(SPL1)	1.279	129.861	0.64	8.27	10.58
NST1(SPL1)	1.041	125.638	0.60	9.14	9.51
NST2(SPL1)	1.188	135.690	0.55	8.12	9.65
NST3(SPL1)	1.295	150.937	0.47	7.06	9.14
SingleT-9 × 9	0.710	94.482	0.46	7.90	5.60
SingleT-6 × 12	0.700	91.329	0.51	8.34	5.83
ART1(SPL1)	0.748	114.275	0.37	7.16	5.36
ART2(SPL1)	0.821	119.092	0.34	6.64	5.45
AV_i	0.973	120.16	0.49	7.83	7.64

Table 6 Positive distance from average (PDA)

Code	Positive_Distance_from_Average (PDA)				
NRT(SPL1)	0	0	0.30	0.06	0.38
NST1(SPL1)	0	0	0.22	0.17	0.24
NST2(SPL1)	0	0	0.12	0.04	0.26
NST3(SPL1)	0	0	0	0	0.20
SingleT-9 × 9	0.27	0.21	0	0.01	0
SingleT-6 × 12	0.28	0.24	0.04	0.07	0
ART1(SPL1)	0.23	0.05	0	0	0
ART2(SPL1)	0.16	0.01	0	0	0

Table 7 Negative distance from average (NDA)

Code	Negative_Distance_from_Average (NDA)				
NRT(SPL1)	0.31	0.08	0	0	0
NST1(SPL1)	0.07	0.05	0	0	0
NST2(SPL1)	0.22	0.22	0	0	0
NST3(SPL1)	0.33	0.26	0.05	0.10	0
SingleT-9 × 9	0	0	0.07	0	0.27
SingleT-6 × 12	0	0	0	0	0.24
ART1(SPL1)	0	0	0.25	0.09	0.30
ART2(SPL1)	0	0	0.31	0.15	0.29

Table 8 SPi, SNi, NSPi and NSNi

Code	SP_i	SN_i	NSP_i	NSN_i
NRT(SPL1)	0.27	0.14	1	0.47
NST1(SPL1)	0.23	0.04	0.85	0.85
NST2(SPL1)	0.15	0.13	0.56	0.53
NST3(SPL1)	0.07	0.26	0.27	0.02
SingleT-9 × 9	0.18	0.12	0.67	0.55
SingleT-6 × 12	0.22	0.09	0.84	0.68
ART1(SPL1)	0.10	0.23	0.38	0.15
ART2(SPL1)	0.06	0.27	0.22	0

Table 9 Ranking of samples

Code	AS_i	Rank
NRT(SPL1)	0.7357	3
NST1(SPL1)	0.8483	1
NST2(SPL1)	0.5473	5
NST3(SPL1)	0.1438	7
SingleT-9 × 9	0.6102	4
SingleT-6 × 12	0.7610	2
ART1(SPL1)	0.2663	6
ART2(SPL1)	0.1113	8

Given the significance of PCL in crashworthiness performance, outer shells exhibiting PCL values exceeding 100 kN were selected for further investigation. These shells were subsequently filled with cores to examine the impact of both tube arrangement and core on crashworthiness performance. The selection process, which was informed by the Sect. 3.3, resulted in the inclusion of several samples for analysis. These samples, as detailed in Table 4, comprise the NST1 optimum shell architecture, as well as the NRT, NST2, NST3, ART1 and ART2 configurations, each

offering unique structural properties that warrant comprehensive examination in crashworthiness design.

3.4 Filled samples

The failure modes and load-displacement characteristics of the investigated samples, as illustrated in Fig. 14, reveal complex deformation processes that are significantly influenced by both structural configuration and core composition. The load response exhibits a distinctive pattern, characterized by an initial peak in the first stage, followed by a transition into a stable phase, before ultimately ascending during the hardening stage. This tripartite deformation process, comprising peak, plateau and hardening stages, is consistently observed across all samples, which uniformly experienced crushing under the applied load.

A notable observation emerges regarding the NRT(FEA) samples, both in their core-filled and non-core-filled configurations, which demonstrate superior crashworthiness indices compared to their NSTi(FEA) and ARTi(FEA) counterparts. However, it is important to acknowledge that ART specimens maintain a mass advantage over NRT configurations, presenting a trade-off between performance and weight efficiency. The evidence suggests that three primary factors—cross-sectional geometry, tube arrangement and core—exert comparable influences on the key performance metrics (PCL, MCL, EA and SEA). Nevertheless, the exceptional enhancement in crashworthiness indices observed in core-filled ART1(FEA) and ART2(FEA) specimens, with improvements in EA up to 94.11% and SEA up to 40.36% compared to their unfilled counterparts (as detailed in Sect. 3.4.5 and 3.4.6), relative to other configurations, underscores the crucial significance of tube arrangement, mass and core filling. Furthermore, comparative analysis indicates that ART2(FEA)_Cj configurations consistently demonstrate superior crashworthiness performance metrics when compared to ART1(FEA)_Cj variants, suggesting potential directions for future design.

A detailed analysis of the failure modes and deformation patterns yields several noteworthy observations that underscore the substantial impact of both structure and core type: (i) Diverse configurations exhibit distinct failure modes and deformation patterns. For example, the ART1(FEA)_Cj samples display a higher number of folds compared to the coreless ART1(FEA), indicating improved energy absorption through localized buckling. (ii) Core-filled samples enhance the crushing resistance and load-carrying capacity of the tubes, as evidenced by their elevated PCL and EA values. For instance, the ART1(FEA)_C2 sample exhibits a PCL of 118.13 kN and an EA of 10.92 kJ, surpassing the coreless ART1(FEA) sample, which achieved a PCL of 113.29 kN and an EA of 5.69 kJ, representing increases of

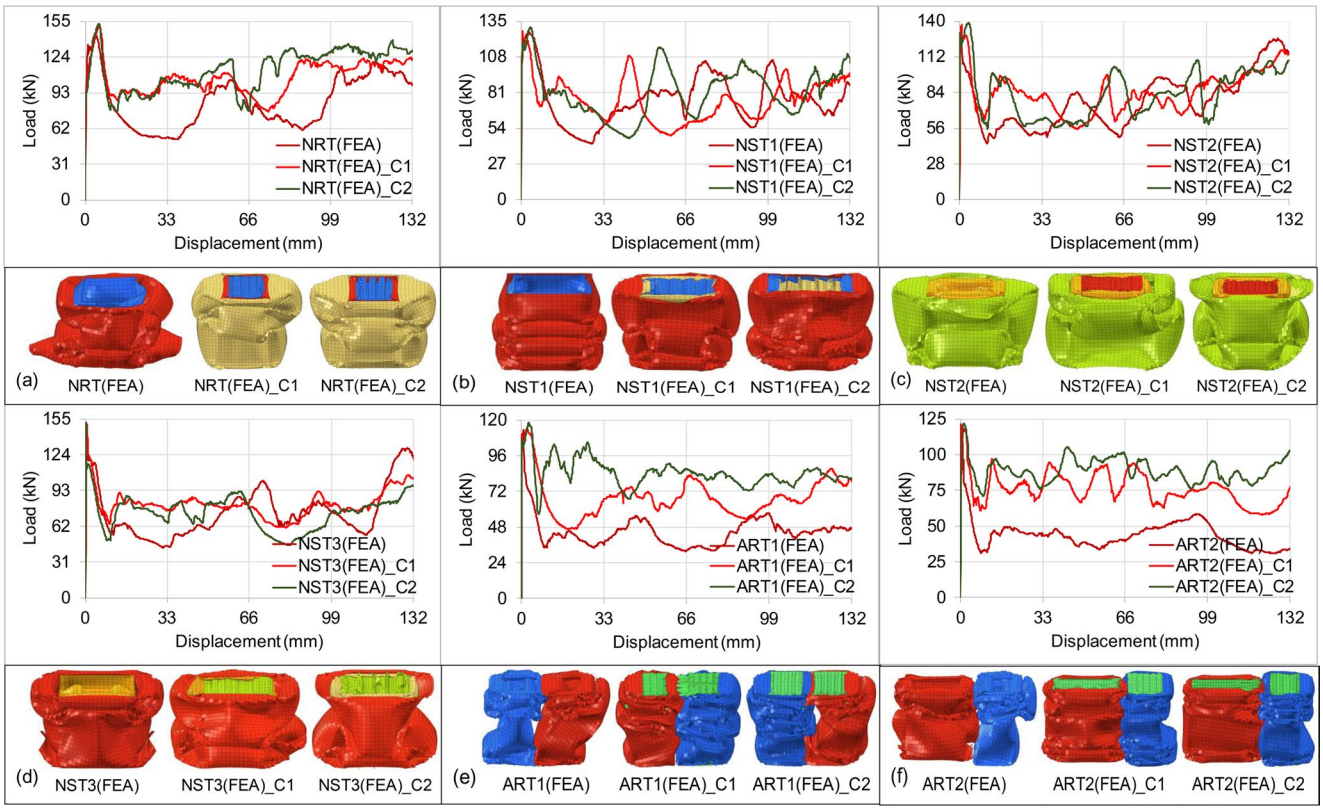

Fig. 14 Behavior of tube without and with cores: (**a**) NRT, (**b**) NST1, (**c**) NST2, (**d**) NST3, (**e**) ART1, and (**f**) ART2

approximately 4.3% in PCL and 92% in EA. Similarly, the NRT(FEA)_Cj cases demonstrate higher load levels and more efficient energy dissipation compared to the unfilled NRT(FEA) configuration.

3.4.1 Interaction between surrounding (inner) shell and core

The "matching effect" in core-filled tubes, defined as the synergistic interaction between the core and surrounding tube that enhances structural stability, load-bearing capacity and energy absorption while promoting uniform deformation, specifically involves the interaction between the core and the surrounding tube, enhancing the structural performance of the tube by improving its stability, load-bearing capacity and energy absorption and allowing for a more uniform deformation [52], which can be observed in Fig. 15(a). When subjected to axial loading, the interaction between the core and the surrounding shell plays a pivotal role in determining the overall mechanical response of the core-filled tube. Two primary interactions are observed: (a) Core-induced shell deformation: The core material forces the folds of the surrounding shell to compress. (b) Shell-constrained core densification: The surrounding shell constrains the core material, leading to its densification (shown in Figs. 14 and 15).

The formation of repeated folds represents a desirable characteristic for energy absorption applications [53]. However, in the studied samples, particularly in core-filled nested tubes, the occurrence of unrepeated folds in the outer shell presents an undesirable outcome. This phenomenon primarily results from reduced interaction between the core and outer shell, especially when compared to the stronger interaction between the inner shell and core, largely attributable to the gap between outer and inner shells. Furthermore, observations from Fig. 15 reveal that shells in direct contact with the core develop a greater number of folds compared to those without core contact.

Chen and Wierzbicki's research [54] demonstrated that energy absorption primarily comprises bending and membrane energies, which depend on the length of plastic hinges and the surrounding membrane areas. In core-filled tubes, both hinge lengths and membrane areas exceed those in unfilled tubes, requiring greater energy for their formation, as shown in Figs. 14 and 16. Building on this observation, a comparative analysis of energy absorption (EA) at a displacement of 120 mm reveals notable differences among configurations. Multi-cell tubes with circular corners [50] and the honeycomb-filled tubes [52] exhibit EAs of approximately 4.02 kJ and 3.63 kJ, respectively, whereas honeycomb-filled square tubes [27] achieve about 5.13 kJ. In contrast, ART(FEA)_C1 attains a significantly higher EA of approximately 7.87 kJ—an improvement of over

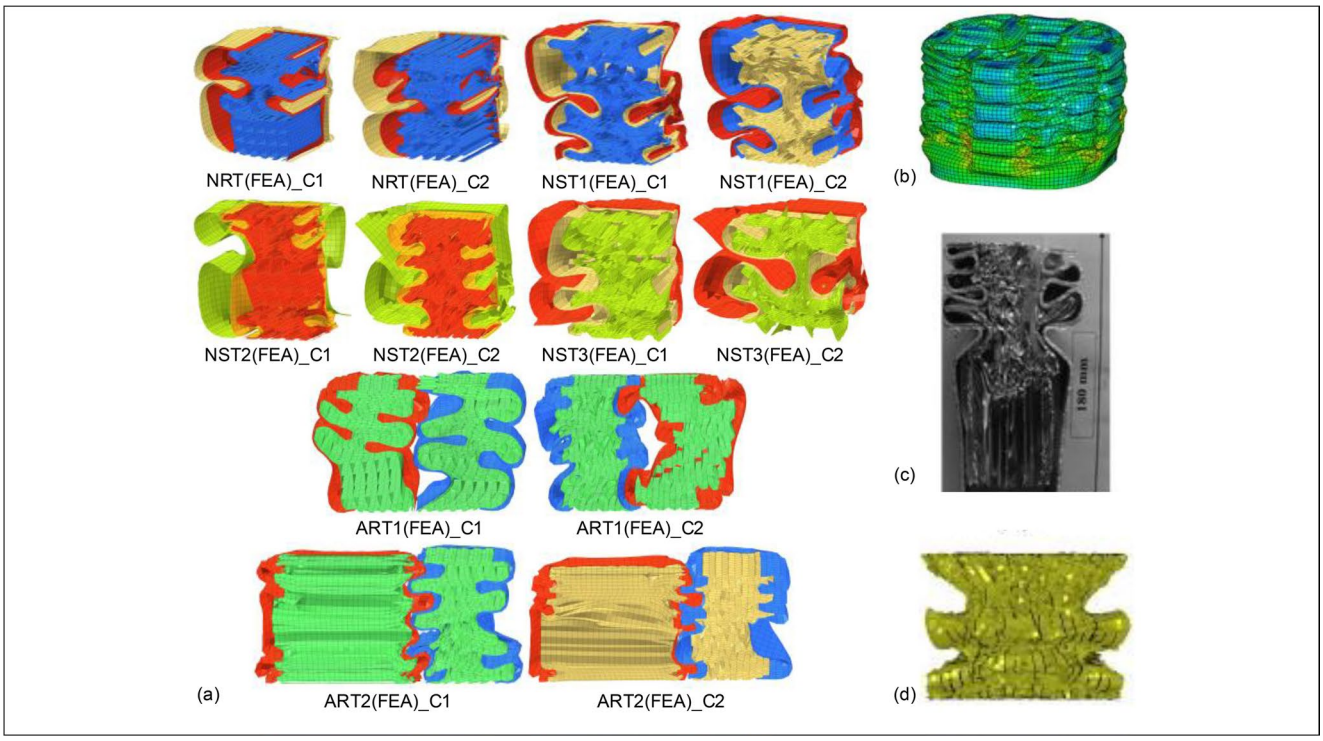

Fig. 15 Interaction between outer shell and core: (**a**) present, (**b**) multi-cell tube with circular corners [50], (**c**) honeycomb-filled tube [52] and (**d**) honeycomb-filled square tube [27]

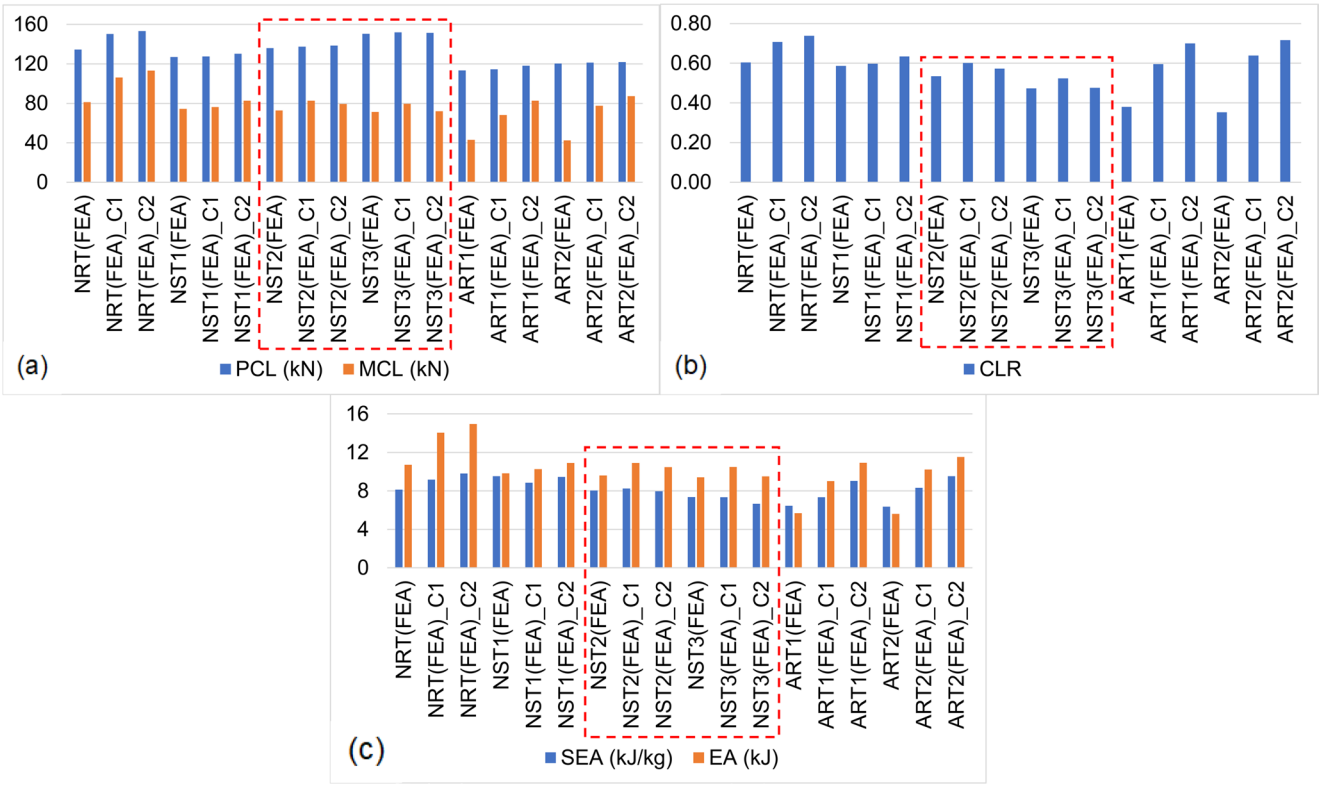

Fig. 16 Effect of tube arrangement and core on: (**a**) PCL and MCL, (**b**) CLR and (c) SEA and EA

50% compared with the best-performing honeycomb-filled square tube [27] —highlighting the novelty and enhanced efficiency achieved through the combination of steel tubes and ABS cores.

3.4.2 Effect of tube arrangement and core for PCL

A comparative analysis of the crashworthiness metrics presented in Fig. 16 reveals significant variations between core-filled and unfilled tubes, highlighting the interplay of tube arrangement and core in determining performance. The data, particularly as illustrated in Fig. 16(a), demonstrates a general trend of higher PCLs in core-filled samples compared to their corresponding unfilled counterparts, underscoring the substantial influence of cores on the initial resistance to deformation. Notably, the PCL enhancement observed in core-filled NRT(FEA) samples is particularly striking, with an average increase of 12.88% compared to the coreless NRT(FEA) configuration. This improvement stands in stark contrast to the more modest average increase of 1.45% observed across other core-filled samples. The disparity in PCL enhancement can be attributed to a combination of factors: the inherent strength of the rectangular section, the interactions between the tube walls within the structure and the supportive role of the core filling in facilitating the formation of perfect folds during deformation.

Further examination of Fig. 16(a) reveals additional nuances in the comparative performance of different configurations. The PCLs of ARTi(FEA)_Cj samples are found to be significantly lower than those of both NRT(FEA)-Cj and NSTi(FEA)_Cj configurations, with the discrepancy ranging from 9.73% to 23.36%. This substantial variation in PCL values across different designs emphasizes the critical role of geometry in determining initial crushing resistance. Moreover, a comparison between the two ART configurations yields another interesting observation: ART2(FEA)_Cj exhibits a PCL approximately 4.46% larger than that of ART1(FEA)_Cj. This difference, while less pronounced than some of the other variations noted, nonetheless underscores the sensitivity of crashworthiness to even relatively minor alterations in design.

3.4.3 Effect of tube arrangement and core for MCL

An examination of MCLs presented in Fig. 16(a) reveals a marked improvement in the performance of core-filled samples across various structural configurations, highlighting the significant impact of cores on sustained crushing resistance. The NSTi(FEA)_Cj samples demonstrate a moderate yet consistent improvement, with MCLs showing an average increase of 8.17% compared to their unfilled counterparts. In contrast, the NRT(FEA)-Cj, ART1(FEA)_Cj and ART2(FEA)_Cj configurations exhibit substantially larger enhancements in

MCLs, with increases ranging from an impressive 35.11% to a remarkable 94.21%. This improvement in MCL can be attributed to two key factors: firstly, the ART(FEA) samples were uniquely filled with ABS core material in both component tubes, whereas the other configurations featured core filling only in the inner tube. Secondly, the inherent superior crushing resistance of the rectangular section further augments the performance of the NRT(FEA) samples, contributing to their exceptional MCL enhancement.

Despite the substantial improvements observed in the ART configurations, it is noteworthy that the ARTi(FEA)_Cj samples still exhibit MCLs approximately 28.09% lower than those of the NRT(FEA)_Cj samples. However, a more comparison reveals that the MCLs of ARTi(FEA)_Cj are comparable to those of NSTi(FEA)_Cj. Furthermore, the ART2(FEA)_Cj configuration demonstrates a slight superiority, with an MCL approximately 1.65% higher than that of NST2(FEA)_Cj. An additional point emerges from the comparison between the two ART configurations: ART2(FEA)_Cj exhibits a 9.18% increase in MCL compared to ART1(FEA)_Cj. This difference underscores the sensitivity of crushing performance to subtle variations in structural design, even within similarly categorized configurations.

3.4.4 Effect of tube arrangement and core for CLR

The ARTi(FEA)_Cj configurations, while exhibiting a CLR approximately 8.3% lower than that of NRT(FEA)_Cj, nonetheless demonstrate superior performance compared to the NSTi(FEA)_Cj samples (Fig. 16(b)). Further examination of the data yields additional insights into this index. Notably, the ART2(FEA)_Cj sample exhibits a CLR surpassing that of NST3(FEA)_Cj by a substantial margin of approximately 35.64%. This significant difference emphasizes the potential for certain structural designs to dramatically outperform others in terms of crash load.

When comparing the two ART configurations, a yet noteworthy distinction emerges: the CLR of ART2(FEA)_Cj shows a 4.63% increase relative to that of ART1(FEA)_Cj. This improvement, while modest, highlights the sensitivity of crash performance to even minor variations in structural design within similar configuration categories. The observed enhancements in CLR across core-filled tubes can be attributed to the corresponding increases in MCL. This relationship between MCL and CLR is of particular significance in the context of passenger safety, as improved CLR values translate to reduced load transfer to vehicle occupants during crash events.

3.4.5 Effect of tube arrangement and core for EA

A comparative analysis of the core-filled samples reveals significant variations in EA enhancement across different configurations (Fig. 16(c)). The NSTi(FEA)_Cj samples exhibit a moderate average improvement of 8.41% in EA compared to their unfilled counterparts. In contrast, the NRT(FEA)_Cj, ART1(FEA)_Cj and ART2(FEA)_Cj configurations demonstrate substantially larger increases in EA, ranging from an impressive 35.47% to a remarkable 94.11%. This marked disparity in EA enhancement emphasizes the critical role of both structural design and core in determining energy absorption capabilities.

The observed enhancement in EA for core-filled tubes, relative to their unfilled counterparts, aligns with findings from previous studies, particularly the conclusion reached by [55], highlighting the potential of core-filling strategies to improve crashworthiness performance. A more comparison among the core-filled tubes reveals that the ARTi(FEA)_Cj configurations generally exhibit lower EA values compared to other tube designs, with differences ranging from 0.26% to 31.26%. However, this trend is not uniform across all comparisons. Notably, the ART2(FEA)_Cj configuration demonstrates superior EA performance in several instances, surpassing the EA values of NST1(FEA)_Cj, NST2(FEA)_Cj, NST3(FEA)_Cj and ART1(FEA)_Cj by 2.78%, 1.69%, 8.77% and 9.06%, respectively.

3.4.6 Effect of tube arrangement and core for SEA

SEA depends on both the structural mass and EA. An analysis of the core-filled samples reveals divergent trends in SEA (Fig. 16(c)). The NSTi(FEA)_Cj configurations demonstrate a modest average decrease of 2.65% in SEA compared to their unfilled counterparts. This reduction, however, is not uniform across all samples, as evidenced by the NST2(FEA)_C1 configuration, which exhibits a slight increase of 2.73% in SEA. In contrast, the NRT(FEA)_Cj, ART1(FEA)_Cj and ART2(FEA)_Cj samples display significantly larger enhancements in SEA, with improvements ranging from a substantial 16.53% to an impressive 40.36%.

A comparative examination of SEA improvements relative to unfilled counterparts yields further insights into this index. Notably, the ART1(FEA)_Cj and ART2(FEA)_Cj configurations demonstrate remarkably superior performance, with SEA improvements 1.62 times and 2.44 times greater than that of NRT(FEA)_Cj, respectively. When comparing SEA among the core-filled tubes, the ARTi(FEA)_Cj configurations, while exhibiting lower SEA values than NRT(FEA)_Cj and NST1(FEA)_Cj by approximately 9.72% and 4.09% respectively, nonetheless outperform NST2(FEA)_Cj and NST3(FEA)_Cj by significant margins of 9.03% and 18.87%. Furthermore, a comparison between the two ART configurations reveals a notable distinction: ART2(FEA)_Cj demonstrates a

9.02% increase in SEA compared to ART1(FEA)_Cj. This substantial improvement, achieved through tube arrangement, emphasizes the sensitivity of crashworthiness to design.

4 Effect of core C2 compared with core C1

The comparative analysis presented in Fig. 16 highlights that specimens filled with core type 2 (C2) exhibit marginally lower mass compared to their core type 1 (C1) counterparts. Despite the slight mass difference, the crashworthiness performance of C2-filled specimens generally surpasses that of C1-filled samples across a range of parameters, with a few exceptions noted in the NST2(FEA) and NST3(FEA) core-filled samples. This trend is particularly evident in the ART2(FEA)_C2 specimen, which demonstrates consistent improvements in all measured crashworthiness indices. Specifically, ART2(FEA)_C2 shows a 0.5% increase in peak crushing load (PCL), a significant 12.67% improvement in mean crushing load (MCL), a 12.11% increase in crushing load ratio (CLR), a 12.53% enhancement in energy absorption (EA) and a notable 14.49% increase in specific energy absorption (SEA) when compared to the ART2(FEA)_C1. These findings suggest that core type 2 provides enhanced structural integrity and energy dissipation capabilities, making it a more efficient option for improving the overall crashworthiness of tube structures. The observed performance improvements in C2-filled specimens can likely be attributed to more favorable material properties, such as better deformation characteristics and energy absorption potential, leading to enhanced crash performance. This underlines the potential of optimizing core filling materials to significantly improve crashworthiness outcomes while maintaining or even reducing the overall mass of the structures.

The results above provide valuable guidance for the design of lightweight and high-performance energy-absorbing components in engineering applications. The demonstrated improvements in SEA and CLR, along with controlled PCL, indicate that the investigated core-filled configurations can effectively dissipate impact energy while limiting transmitted loads. These characteristics are particularly beneficial for automotive crash boxes, aerospace impact absorbers and protective structures, where minimizing peak loads and maximizing energy absorption are essential for occupant safety and structural integrity. Furthermore, the insights obtained from the Entropy–EDAS evaluation and machine learning predictions offer a useful framework for optimizing future crashworthy designs with enhanced energy efficiency and material utilization.

5 Conclusion

This study combined experimental, numerical and machine learning approaches to investigate the effects of tube arrangement and core type on the crashworthiness of unfilled and ABS core-filled multi-tube structures.

For unfilled structures, both tube arrangement and cross-sectional design were found to strongly influence crashworthiness, with the deformation of the inner tube dictating the overall collapse behavior in nested configurations. The Entropy–EDAS method identified the NST1 configuration as the most efficient among the unfilled designs.

For core-filled structures, crashworthiness was mainly governed by tube arrangement, cross-section and core type. The C2 core exhibited superior performance compared with C1, with the ART2(FEA)_C2 configuration showing significant improvements across all indices, including mean crushing load (MCL), crushing load ratio (CLR) and specific energy absorption (SEA).

Overall, perpendicular ART arrangements—particularly those combining high-modulus steel tubes with low-modulus ABS cores—demonstrated the most favorable balance between strength and energy absorption. These findings provide valuable design guidance for developing lightweight, energy-efficient crashworthy structures in transportation and protective engineering applications. Future work could explore crashworthiness under dynamic loading conditions to assess performance at higher strain rates and investigate alternative core materials, such as polymer composites or hybrid lattices, to further optimize energy absorption and weight reduction.

Acknowledgements Thanks to Van Lang University for supporting this work.

Author contributions Conceptualization, formal analysis and article writing by ThanhSon Doan and Trong Nhan Tran; numerical simulations by Arun Arjunan and Ameen Topa; analysis of numerical simulation and methodology by Quirino Estrada; methodology and discussion of results by PhucThien Nguyen and Arun Arjunan.

Data availability Data available on request.

Declarations

Ethical approval Not applicable.

Consent to participate Not applicable.

Consent for publication The authors give permission for the publication of this article.

Competing interests The authors declare that they have no conflict of interest.

References

1. Pirmohammad S, Marzdashti SE (2016) Crushing behavior of new designed multi-cell members subjected to axial and oblique quasi-static loads. Thin-Walled Structures 108:291–304
2. Xiao Y, Wu QW, Liu Y, Wang YJ, Long H, Hu HL (2024) Optimization design of crashworthiness of polyurethane foam filled Origami thin wall square tube based on an surrogate model. Struct 65:106713
3. Ge C, Gao Q, Wang L (2018) Theoretical and numerical analysis of crashworthiness of elliptical thin-walled tube. Int J Mech Sci 148:467–474
4. Ha NS, Pham TM, Chen W, Hao H, Lu G (2021) Crashworthiness analysis of bio-inspired fractal tree-like multi-cell circular tubes under axial crushing. Thin-Walled Struct 169:108315
5. Qin S, Deng X, Liu F (2024) Energy absorption characteristics and crashworthiness of rhombic hierarchical gradient multicellular hexagonal tubes. Mech Adv Mater Struct 31:783–804
6. Yang F, Deng X (2024) Study on the crashworthiness of star-shaped multicellular tubes. Mech Adv Mater Struct 31:4880–4897
7. Zhang Z, Sun W, Zhao Y, Hou S (2018) Crashworthiness of different composite tubes by experiments and simulations. Compos Part B Eng 143:86–95
8. Abramowicz W, Jones N (1986) Dynamic progressive buckling of circular and square tubes. Int J Impact Eng 4:243–270
9. Szlosarek R, Luft J, Wittig F, Ullmann M, Prahl U, Kawalla R, Kröger M (2021) Improving the crashworthiness of magnesium AZ31 by tapering and triggering. Thin-Walled Structures 162:107565
10. Zarei HR, Kröger M (2006) Multiobjective crashworthiness optimization of circular aluminum tubes. Thin-Walled Struct 44:301–308
11. Jin M, Hou X, Yin G, Yao R, Gao J, Deng Z (2022) Improving the crashworthiness of bio-inspired multi-cell thin-walled tubes under axial loading: experimental, numerical theoretical studies. Thin-Walled Struct 177:109415
12. Abdulqadir SF, Bassam A, Ansari MNM, Topa A (2021) Design of frontal longitudinal for enhancement in crashworthiness performance. IOP Conf Ser Mater Sci Eng 1128:012026
13. Pirmohammad S, Vosoughifard E (2024) Crashworthiness behavior of multi-cell structures reinforced with small tubes under axial and inclined loading. Mech Based Des Struct Mach 52(12):10783–10808
14. Wu J, Zhang Y, Li J, Lai X, Duan N (2022) Energy absorption characteristics of nested corrugated-elliptical tubes subjected to a lateral crushing load. Compos Struct 297:115926
15. Mustaffa Z, Al-Qadami EHH, Topa A, Budiman BA, Mohd Hamka NA, Bayu Endrayana D, Dharmowijoyo MA (2024) Mohammad Razi, numerical assessment of the side impacts on lithium-ion battery module integrated with honeycomb reinforcement. Eng Fail Anal 161:108290
16. Khaire N, Tiwari G, Rathod S, Iqbal MA, Topa A (2022) Perforation and energy dissipation behaviour of honeycomb core cylindrical sandwich shell subjected to conical shape projectile at high velocity impact. Thin-Walled Structures 171:108724
17. Kim DK, Looi CK, Topa A, Cho NK (2024) Prediction of mechanical response of hexagonal honeycomb SPS blast wall under explosive loading: in-depth review and empirical formula. Ocean Eng 293:116578
18. Gungor E, Topa A, Kucukyıldırım B Numerical Investigation of Innovative Honeycomb-composite Sandwich Structure under Bird-strike Event, 6th International Conference on Advances in Mechanical Engineering 2021
19. Hou S, Li Q, Long S, Yang X, Li W (2007) Design optimization of regular hexagonal thin-walled columns with crashworthiness criteria. Finite Elem Anal Des 43:555–565
20. Tran T, Hou S, Han X, Nguyen N, Chau M (2014) Theoretical prediction and crashworthiness optimization of multi-cell square tubes under oblique impact loading. Int J Mech Sci 89:177–193
21. Usta F, Türkmen HS (2019) Experimental and numerical investigation of impact behavior of nested tubes with and without honeycomb filler. Thin-Walled Struct 143:106256
22. Qin R, Wang X, Gao F, Chen B (2021) Energy absorption performance of hexagonal multi-cell tube with hierarchy under axial loading. Thin-Walled Struct 169:108392
23. Fang J, Gao Y, Sun G, Zhang Y, Li Q (2014) Crashworthiness design of foam-filled bitubal structures with uncertainty. Int J Non-Linear Mech 67:120–132
24. Alavi Nia A, Chahardoli S (2016) Mechanical behavior of nested multi-tubular structures under quasi-static axial load. Thin-Walled Struct 106:376–389
25. Acar E, Altin M, Güler MA (2019) Evaluation of various multicell design concepts for crashworthiness design of thin-walled aluminum tubes. Thin-Walled Struct 142:227–235
26. Reddy TY, Wall RJ (1988) Axial compression of foam-filled thin-walled circular tubes. Int J Impact Eng 7:151–166
27. Wang Z, Yao S, Lu Z, Hui D, Feo L (2016) Matching effect of honeycomb-filled thin-walled square tube—experiment and simulation. Compos Struct 157:494–505
28. Kucewicz M, Baranowski P, Małachowski J, Popławski A, Płatek P (2018) Modelling, and characterization of 3D printed cellular structures. Mater Des 142:177–189
29. Kucewicz M, Baranowski P, Stankiewicz M, Konarzewski M, Płatek P, Małachowski J (2019) Modelling and testing of 3D printed cellular structures under quasi-static and dynamic conditions. Thin-Walled Structures 145:106385
30. Bates SRG, Farrow IR, Trask RS (2019) Compressive behaviour of 3D printed thermoplastic polyurethane honeycombs with graded densities. Mater Des 162:130–142
31. Dar UA, Mian HH, Abid M, Topa A, Sheikh MZ, Bilal M (2020) Experimental and numerical investigation of compressive behavior of lattice structures manufactured through projection micro stereolithography. Mater Today Commun 25:101563
32. Kumar R, Kumar A, Ranjan Kumar D (2023) Buckling response of CNT based hybrid FG plates using finite element method and machine learning method. Compos Struct 319:117204
33. Duong HT, Phan HC, Tran TM, Dhar AS (2021) Assessment of critical buckling load of functionally graded plates using artificial neural network modeling. Neural Comput Appl 33:16425–16437
34. Aggarwal A, Choudhary C, Mehrotra D (2018) Evaluation of smartphones in Indian market using EDAS. Procedia Comput Sci 132:236–243
35. Tabacu S, Ducu C (2018) Experimental testing and numerical analysis of FDM multi-cell inserts and hybrid structures. Thin-Walled Struct 129:197–212
36. Wang K, Sun G, Wang J, Yao S, Baghani M, Peng Y (2023) Reversible energy absorbing behaviors of shape-memory thin-walled structures. Eng Struct 279:115626
37. Breiman L, Forests R (2001) Mach Learn 45:5–32
38. Mehreganian N, Louca LA, Langdon GS, Curry RJ, Abdul-Karim N (2018) The response of mild steel and armour steel plates to localised air-blast loading-comparison of numerical modelling techniques. Int J Impact Eng 115:81–93
39. Marangoni AL, Massaroppi E (2017) Cowper-symonds parameters estimation for ABS material using design of experiments with finite element simulation. Polímeros 27:220–224
40. Le D, Doan T, Do K, Dang V, Pham H, Tran T (2023) Investigating and comparing the mechanical behavior of multicellular

structures made with PLA and ABS under lateral loading. Proc Inst Mech Eng Part L J Mater Des Appl 237(9):1952–1963
41. Simpson J, Kazancı Z (2020) Crushing investigation of crash boxes filled with honeycomb and re-entrant (auxetic) lattices. Thin-Walled Struct 150:106676
42. Langseth M, Hopperstad OS (1996) Static and dynamic axial crushing of square thin-walled aluminium extrusions. Int J Impact Eng 18:949–968
43. Haghi Kashani M, Shahsavari Alavijeh H, Akbarshahi H, Shakeri M (2013) Bitubular square tubes with different arrangements under quasi-static axial compression loading. Mater Des 51:1095–1103
44. Jensen Ø, Langseth M, Hopperstad O (2005) Transition from progressive to global buckling of aluminium extrusions – a numerical study. Int J Crashworthiness 10:609–620
45. Akhavan Attar A, Kazemi M (2022) Novel geometric arrangement effects on energy absorption of a conical structure with various cross-sections. Thin-Walled Struct 173:109005
46. Du Z, Duan L, Cheng A, Wei B, Zhang G (2021) Theoretical prediction and analysis of hybrid material hat-shaped tubes with strengthened corner structures under quasi-static axial loading. Eng Struct 230:111699
47. Hou S, Han X, Sun G, Long S, Li W, Yang X, Li Q (2011) Multiobjective optimization for tapered circular tubes. Thin-Walled Struct 49:855–863
48. Sun G, Li S, Liu Q, Li G, Li Q (2016) Experimental study on crashworthiness of empty/aluminum foam/honeycomb-filled CFRP tubes. Compos Struct 152:969–993
49. Schneider F, Jones N (2004) Impact of thin-walled high-strength steel structural sections. Proc Inst Mech Eng Part D J Automob Eng 218:131–158
50. Chen S, Yu H, Fang J (2018) A novel multi-cell tubal structure with circular corners for crashworthiness. Thin-Walled Structures 122:329–343
51. Yin H, Wen G, Hou S, Qing Q (2013) Multiobjective crashworthiness optimization of functionally lateral graded foam-filled tubes. Materials & Design (1980-2015) 44:414–428
52. Zarei H, Kröger M (2008) Optimum honeycomb filled crash absorber design. Mater Des 29:193–204
53. Chen J, Li E, Liu W, Mao Y, Hou S (2024) Crashworthiness analysis of novel cactus-inspired multi-cell structures under axial crushing. Int J Mech Sci 268:109053
54. Chen W, Wierzbicki T (2001) Relative merits of single-cell, multicell and foam-filled thin-walled structures in energy absorption. Thin-Walled Struct 39:287–306
55. Wang Z, Liu J (2018) Mechanical performance of honeycomb filled with circular CFRP tubes. Compos Part B Eng 135:232–241